WILEY

REVIEW ARTICLE

Interface engineering of inorganic solid-state lithium batteries via atomic and molecular layer deposition

Huaihu Sun[1] | Hongliu Dai[2] | Gaixia Zhang[2] | Shuhui Sun[1]

[1]Institut National de la Recherche Scientifique (INRS), Centre Énergie Matériaux Télécommunications, Varennes, Québec, Canada

[2]Department of Electrical Engineering, École de Technologie Supérieure (ÉTS), Montréal, Québec, Canada

Correspondence
Gaixia Zhang, Department of Electrical Engineering, École de Technologie Supérieure (ÉTS), Montréal, Québec, H3C 1K3, Canada.
Email: gaixia.zhang@etsmtl.ca

Shuhui Sun, Institut National de la Recherche Scientifique (INRS), Centre Énergie Matériaux Télécommunications, Varennes, Québec, J3X 1P7, Canada.
Email: shuhui.sun@inrs.ca

Abstract

Currently, conventional organic liquid electrolytes (OLEs) are the main limiting factor for the next generation of high-energy lithium batteries. There is growing interest in inorganic solid-state electrolytes (ISEs). However, ISEs still face various challenges in practical applications, particularly at the interface between ISE and the electrode, which significantly affects the performance of solid-state batteries (SSBs). In recent decades, atomic and molecular layer deposition (ALD and MLD) techniques, widely used to manipulate interface properties and construct novel electrode structures, have emerged as promising strategies to address the interface challenges faced by ISEs. This review focuses on the latest developments and applications of ALD/MLD technology in SSBs, including interface modification of cathodes and lithium metal anodes. From the perspective of interface strategy mechanism, we present experimental progress and computational simulations related to interface chemistry and electrochemical stability in thermodynamic contents. In addition, this article explores the future direction and prospects for ALD/MLD in dynamic stability engineering of interfaces SSBs.

KEYWORDS
atomic layer deposition, inorganic solid-state electrolytes, interface modification, molecular layer deposition, solid-state batteries

1 | INTRODUCTION

Among many energy storage devices, lithium-ion batteries (LIBs) have revolutionized mobile phones, laptops and other electronic markets as well as electric vehicles (EVs) and energy storage, since their commercialization by Sony in the 1990s.[1] The high specific energy and high power density of LIBs are mainly due to the low density of lithium (0.53 g cm^{-3}), the small radius of lithium ion (0.76 Å), and the lower oxidation–reduction potential compared with other alkali metal elements.[2–4] These characteristics make LIBs widely utilized in the field of portable electronic devices and EVs, offering significant commercial value. However, the flammable liquid electrolyte used in LIBs and their limited energy density diminishes their potential in the future energy market.[5] In contrast, the inorganic all-solid-state lithium batteries (IASSLBs), which utilize high-capacity (3860 mAh g^{-1})

Huaihu Sun and Hongliu Dai contributed equally to this work.

lithium (Li) metal and nonflammable inorganic solid-state electrolytes (ISEs), are expected to meet the urgent needs of the next-generation of energy solutions by significantly improving the energy density and safety.[6]

The main ISEs used in IASSLBs are divided into perovskite-type, β-Al$_2$O$_3$-type, NASICON-type, garnet-type, sulfide-type, hydride type, and antiperovskite type.[7] ISEs offer several significant advantages due to their distinct properties: (1) In terms of physical properties, ISEs, such as Li$_3$xLa$_2$/$_{3-x}$TiO$_3$, demonstrate relatively high ionic conductivity at room temperature, typically around 10^{-3} S cm^{-1}. This level of conductivity is critical for efficient ion transport within the battery, ensuring rapid charge and discharge cycles. Additionally, these electrolytes exhibit excellent mechanical properties, which help maintain structural integrity and prevent mechanical failure under operational conditions; (2) In terms of chemical and electrochemical properties, ISEs have a wide electrochemical window (>4.0 V), which allows the electrolytes to operate effectively over a broad range of voltages without undergoing detrimental side reactions or decomposition. Furthermore, these materials exhibit robust oxidation stability, contributing to their safety and longevity in battery applications; 3) In terms of thermodynamic properties, ISEs are characterized by a wide working temperature range, from as low as $-30°$C to as high as $300°$C.[8] This extensive temperature tolerance ensures that the electrolytes can function reliably in diverse environmental conditions, making them suitable for a range of applications that require stable performance across varying temperatures. ISEs also protect the normal operation of the battery in high and low-temperature environments (e.g., $-50°$C to $200°$C or higher), while traditional liquid electrolytes may freeze, boil, or decompose.[9] Although inorganic SSEs have many advantages, IASSLB based on ISEs face several obstacles in realizing the same practical application as LIBs. For example, although the low activation energy of fast ion conduction in ISE helps to maintain the high ion conductivity of electrolyte at low temperature, the high resistance at the interface between electrolyte and electrode still hinders the transmission of Li$^+$ ion due to poor contact and leads to the failure of IASSLBs.[10] Besides, there are also manufacturing difficulties (such as large area vulnerability), low coulombic efficiency (CE), risks of battery misfire caused by metal dendrite growth and diffusion along the grain boundary under low current density, side reactions at the interface and stress/strain changes, high cost and poor environmental stability.[11–15] Therefore, analyzing and overcoming general interface issues in IASSLBs will have a significant positive impact on the advancement of solid-state electrochemical energy storage devices in the future.

To date, various synthesis strategies have been employed to enhance the (electrochemical) stability of electrode/ISE interface materials. These include solid-state reactions, mechanochemistry, melt quenching, wet chemical processes (a more recent approach), physical vapor deposition (PVD), pulsed laser deposition (PLD), chemical vapor deposition (CVD), electron beam evaporation, magnetron sputtering, and spray drying.[24–32] These methods typically require constant efforts to optimize compound compositions through experiments to achieve the most favorable ionic conductivity, which can greatly complicate the operation process. In this context, atomic/molecular layer deposition (ALD/MLD) is an advantageous method. It allows precise control over compound composition and accelerates the search for high-quality materials (Figure 1). Notably, in film deposition, ALD/MLD, which reply on surface chemical saturation and the self-limiting reactions, can produce films with an exceptionally high degree of uniformity, even structures with high aspect ratios.[33–35] Furthermore, compared to other deposition technologies, ALD/MLD offers several advantages: (i) precise control over crystallinity and composition, (ii) excellent shape retention on the 3D surfaces, (iii) significant chemical selectivity, and (iv) remarkable scalability (Table 1).[36–38]

In this review, we summary the latest development of ALD/MLD technology for the application in solid-state batteries, focusing particularly on interface regulation in IASSLBs. Specifically, we first briefly introduce ALD/MLD technology, then summary the interface barriers of ALD/MLD for IASSLBs and analyze the interface modification mechanisms. In the final section, we present our perspective on the further advancement and application of ALD/MLD in IASSLBs.

2 | ROLE OF ALD/MLD

Suntola and Antson reported for the first time in the 1970s a vapor-phase film technology called atomic layer epitaxy (ALE) for synthesizing polycrystalline ZnS films for electroluminescent displays.[41,42] Since then, the urgent demand for continuous and pinhole-free films in the microelectronics industry and nanotechnology has enormously promoted the progress of this technology, as evidenced by the sharp increase in the number of new technologies (such as spatial ALD, particle ALD, and low-temperature ALD).[43–48] Later, the name of the technology was changed to ALD because most of the films grown on the substrate did not undergo the epitaxial process, but through the sequential self-limited surface reaction. Benefiting from ALD's excellent shape retention on high aspect ratio structures, precise angstrom level
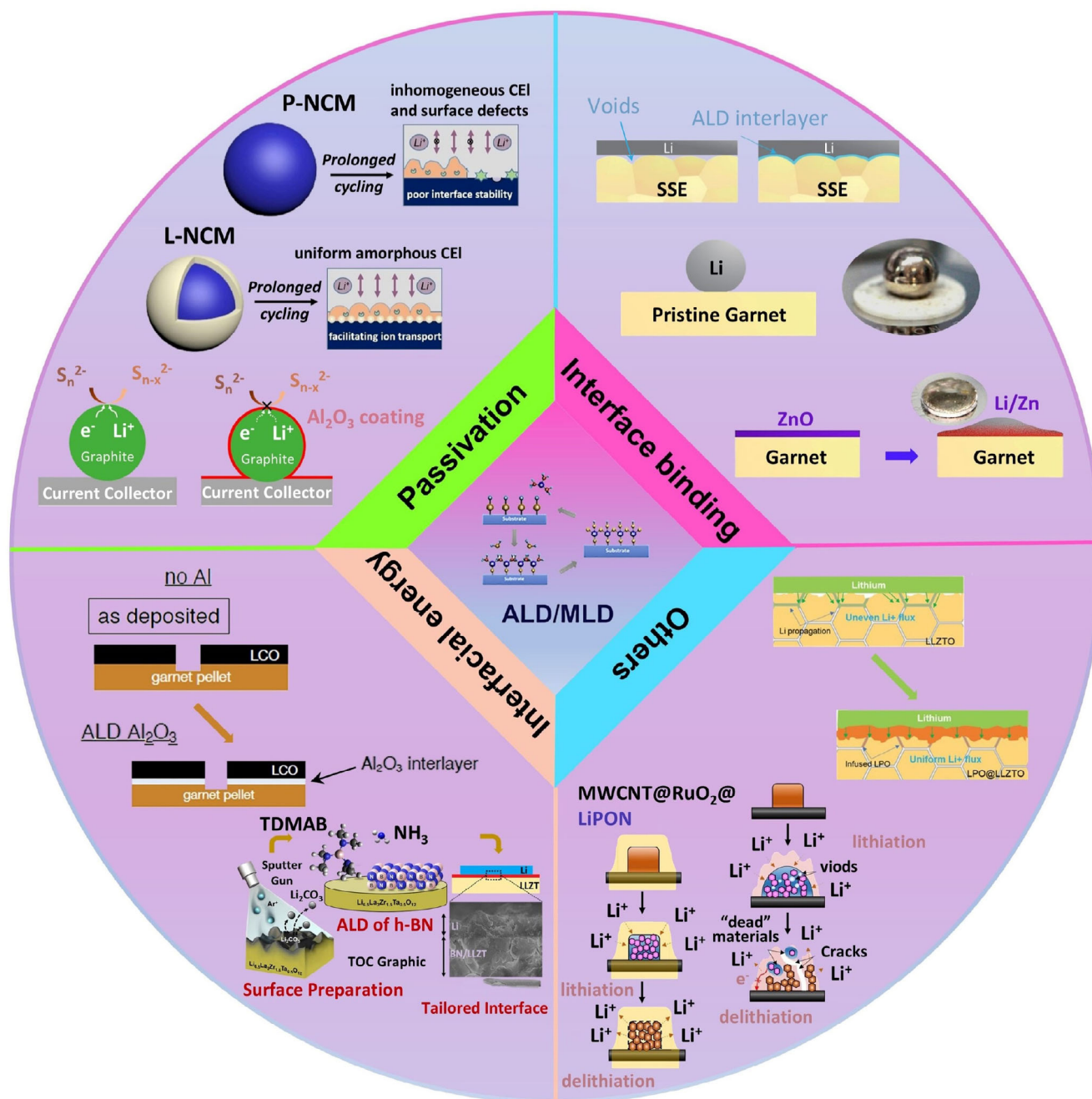
FIGURE 1 Schematic diagram: Many applications of ALD/MLD were employed on solid-state batteries containing metal anode. Pictures are reproduced with permission from: Copyright 2022,[16] Wiley-VCH; Copyright 2018,[17] American Chemical Society; Copyright 2016,[18] Springer Nature; Copyright 2017,[19] American Chemical Society; Copyright 2022,[20] IOP Publishing; Copyright 2021,[21] American Chemical Society; Copyright 2020,[22] Wiley-VCH; Copyright 2016,[23] American Chemical Society.

thickness control, and adjustable film composition, ALD-related research has expanded to the design of various precursors,[49] and the development of new materials such as oxides, nitrides, sulfides, fluorides, metals, doping, and multicomponent compounds.[50,51] The advancement of new processes, including planar substrates, complex substrates, powder surface ALD processes, and roll-to-roll ALD processes, has greatly enriched the materials and

processes available in the ALD toolbox, enabling the application of ALD technology across an increasing number of fields.[52,53] Today, ALD has become a powerful tool for many industrial and research applications, including microelectronics, energy, and information technologies.[54] The origins of MLD can be traced back to the synthesis of pure organic polyimide polymers, slightly later than ALD.[55,56] However, MLD not only inherits the

TABLE 1 Comparison of advantages of different synthetic deposition technologies.

Method	Homogeneity and smoothness	Conformality	Single atomic layer film	Controllable thickness	Completely dense deposit	References
Solution method	Inferior	Impossible	Impossible	Impossible	Impossible	39
Sol–gel method	Inferior	Impossible	Impossible	Impossible	Impossible	39
Chemical vapor deposition (CVD)	Variant	Variant	Impossible	Superior	Superior	25
Physical vapor deposition (PVD)	Mediocre	Only applicable to flat samples	Impossible	Superior	Superior	29
Pulsed laser deposition (PLD)	Mediocre	Only applicable to flat samples	Impossible	Superior	Superior	30
Atomic/molecule layer deposition (ALD/MLD)	Superior	Superior	Superior	Superior	Superior	40

advantages of ALD in terms of uniformity, shape preservation and controllability, but also significantly expands the range of precursors and final products. These include polyimide, polyamide, polyurea, and cross-linked carbosiloxane, and organic–inorganic hybrid materials using zinc, titanium, and vanadium metal precursors.[34,57–61] MLD technology has received increasing attention for its precise regulation of the growth of organic–inorganic hybrid films. In recent years, MLD has demonstrated great potential for applications such as microelectronics, catalysis, energy storage devices, and light-emitting devices.[62–64]

More specifically, the latest advancements in ALD and MLD have significantly promoted the development of IASSLBs, offering promising solutions to the challenges of energy storage. ALD and MLD technologies enable precise control over thin film deposition at the atomic level, which is crucial for creating uniform and defect-free interfaces in IASSLBs. This precision enhances the stability, efficiency, and overall performance of the batteries, particularly in terms of improving ion conductivity and preventing dendrite formation, which is a common issue in lithium-based batteries. Recent research has demonstrated the successful application of ALD/MLD in synthesizing advanced solid electrolytes and protective coatings that can withstand harsh conditions within a battery, thereby extending its lifecycle and safety.

The potential of ALD and MLD for large-scale applications is also considerable, especially as these technologies can be tailored to accommodate a wide range of materials and complex geometries. Their ability to deposit thin films conformally on high-aspect-ratio structures makes them ideal for the mass production of solid-state batteries. Moreover, the scalability of ALD/MLD processes, including roll-to-roll manufacturing and powder surface coating techniques, suggests that these technologies could be integrated into existing battery production lines, thus reducing costs and enhancing commercial viability.

However, despite these exciting advancements, there are still several limitations that must be addressed before ALD and MLD can be widely adopted for IASSLBs. For example, (i) the relatively slow deposition rates can lead to longer production times and increased costs; (ii) the development of suitable precursors for a broader range of materials remains a critical bottleneck; and (iii) the compatibility of ALD and MLD processes with various substrate materials and the need for high-temperature stability in some applications also pose significant hurdles. A critical examination of current limitations reveals that while ALD and MLD offer substantial benefits for IASSLBs, further research and development are necessary to overcome these challenges and fully realize the technology's potential for large-scale application.

ALD/MLD is a kind of thin film preparation technology that grows layer by layer at an atomic level. In the ideal ALD growth process, different precursors are exposed to the surface of the substrate through selective alternation, and the deposition film is formed by chemical adsorption and reaction on the surface. As opposed to conventional CVD, ALD/MLD technology strictly employs alternating pulse precursors to prevent gas-phase reactions. A complete ALD/MLD growth cycle can be divided into four steps:[65]

1. The first precursor of the pulse is exposed to the surface of the substrate, and the first precursor is chemically adsorbed on the surface of the substrate;
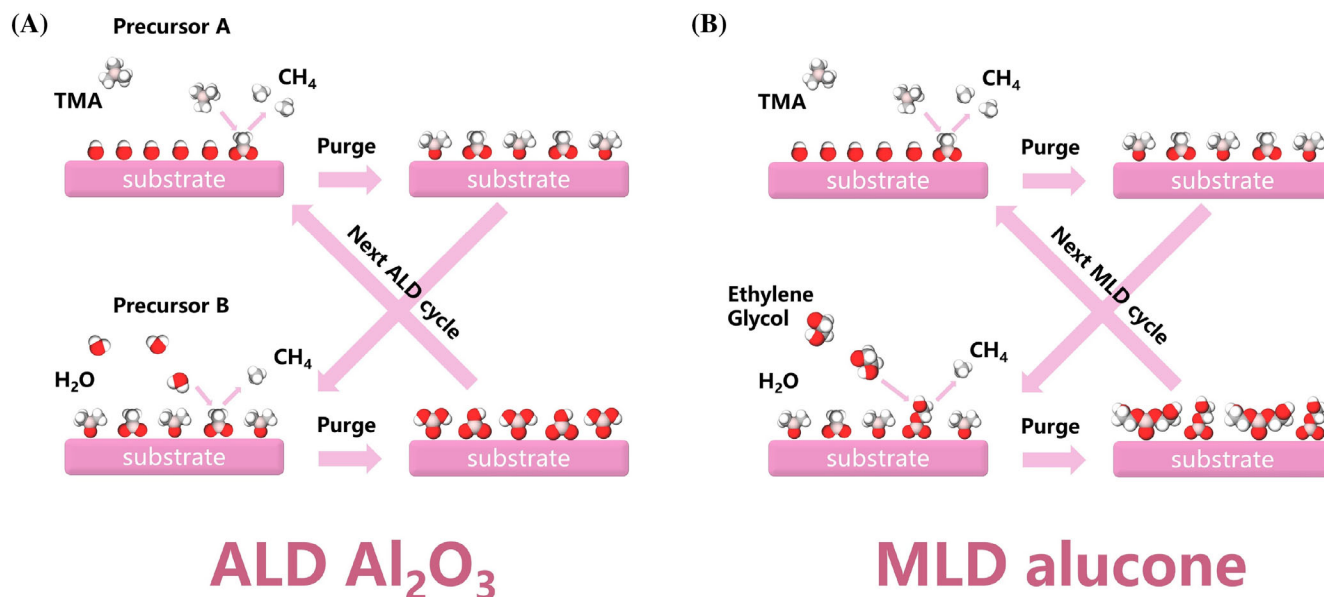2. Inert carrier gas blows away the remaining unresponsive precursor;

(A)

ALD Al$_2$O$_3$

(B)

MLD alucone

FIGURE 2 Schematic diagrams of (A) ALD for inorganic films and (B) MLD for hybrid inorganic–organic films. Reproduced with permission.[66] Copyright 2021, Royal Society of Chemistry.

3. Pulse the second precursor to conduct a chemical reaction on the surface to obtain the required film material;

4. Inert carrier gas blows away the remaining precursors and reaction by-products.

After that, the film deposition with controllable thickness at the atomic scale can be realized by setting the number of cycles or time as depicted in Figure 2. Among them, the first precursor in the ALD process is trimethylaluminum (C_3H_9Al, TMA), and the second precursor is deionized water. The first precursor in the MLD process is also TMA, and the second precursor is ethylene glycol (($CH_2OH)_2$, EG).

For the purpose of this paper, we summary the ALD/MLD conditions used to improve the electrochemical performance of the interface between SSE and electrode (see Table 2). Table 2 collects coating materials with different chemical compositions, including binary oxides (Al_2O_3, $Cr-Al_2O_3$, ZrO_2, ZnO, and HfO_2), lithium ternary oxides ($LiNbO_3$, Li_3NbO_4, Li-Nb-O, Li_3PO_4, and Li_2ZrO_3), borates (Li_3BO_3-Li_2CO_3 and hexagonal boron nitride (h-BN)), and organic compounds (poly(3,4-ethylenedioxythiophene) (PEDOT), Alucone, $Li_{1.5}C_2O_{1.8}$, $Li_2C_8H_4O_4$, and $Li_2C_8H_4O_4$). Table 2 also details the properties of the ALD layers such as the growth per cycle (GPC, ND represents not detect), details of ALD operation specifics, and electrochemical performance of pretreated SSE/electrode configuration. In the following, we comprehensively summarize the interface obstacles in SSE and each type

of interface improvement mechanism prepared using ALD/MLD technology.

3 | INTERFACIAL OBSTACLES IN ISEs

The development of ISEs is extremely rapid, and the room temperature ionic conductivity of most ISEs can meet the actual application requirements.[88] However, the interface between electrodes and ISEs is still the key and difficult point. Firstly, compared with liquid electrolytes, the wettability between ISEs and electrode surface is poor, resulting in the limited actual contact area between each other and further forming solid–solid interface contact inside the battery, weakening the interface contact performance. Moreover, in the process of Li^+ continuous insertion/removal, ISEs cannot cope with the volume change of electrode material, resulting in the continuous deterioration of interface contact and finally, the ultrahigh interface impedance, which will make it difficult for SSBs to achieve the same high- rate charging/discharging and long cycle life as the liquid battery.[89–91] To make further breakthroughs, SSBs need to improve their own "short board", and the interface problem between ISEs and electrodes is the biggest short board of the SSB systems at present. With the deepening of research, the current mainstream ISEs/electrode interface problems can be classified into the following categories: Lithium dendrites, interface reactions, electrochemical instability, and poor physical contact (Figure 3).[9]

TABLE 2 Summary of ALD/MLD for the modification of interface between SSEs and electrodes.

Method	Electrode/SSEs	Layer materials	Precursor	Temp. (°C)	GPC (Å)	Electrochemical performance before	Electrochemical performance after	References
ALD	$LiCoO_2/Li_{3.15}Ge_{0.15}P_{0.85}S_4$	Al_2O_3	TMA/H_2O	400	ND	Retention of 70% after the 25th cycle	Retention of 90% after the 25th cycle	[67]
	$Li/Li_{6.75}La_{2.75}Ca_{0.25}Zr_{1.75}Nb_{0.25}O_{12}$	Al_2O_3	TMA/H_2O	150	1.3	Unable to operate	No polarization of symmetrical cells after 90th cycle	[18]
	$Li/Li_{1.3}Al_{0.3}Ti_{1.7}(PO_4)_3$	Al_2O_3	TMA/H_2O	250	1	Overpotential reaches 3.5 V after 300th cycle	Overpotential less than 0.9 V after 300th cycle	[68]
	$LiCoO_2/Li_7La_{2.75}Ca_{0.25}Zr_{1.75}Ta_{0.25}O_{12}$	Al_2O_3	TMA/H_2O	280	0.1	Discharge capacities less than 4 mAh g^{-1} at 0.08 C	Discharge capacities up to 90 mAh g^{-1} at 0.08 C	[20]
	$Li/Li_{10}GeP_2S_{12}$	Al_2O_3	TMA/H_2O	60	1	The impedance had increased by more than an order of magnitude after several days	The impedance stabilizes at ∼400 Ohm cm^{-2} after several days	[69]
	Li/PEO-LiTFSI SPE	Al_2O_3	TMA/H_2O	100	1	Short circuit within 250 h	Overpotential reaches 37 mV after 500 h	[70]
	$Li/Li_{1+x}Al_xGe_{2-x}(PO_4)_3$	$Cr-Al_2O_3$	$Cr, TMA/H_2O$	150	0.1	Overpotential reaches 2.0 V after 25 h	Overpotential reaches 2.0 V after 850 h	[71]
	$LiNi_{0.8}Mn_{0.1}Co_{0.1}O_2/Li_{10}GeP_2S_{12}$	$LiNbO_3$	$(CH_3)_3COLi/Nb(OC_2H_5)_5$	235	2	20 mAh g^{-1} after 50th cycle	99 mAh g^{-1} after 50th cycle	[72]
	$LiNi_{0.8}Mn_{0.1}Co_{0.1}O_2/Li_{10}SnP_2S_{12}$	$LiNbO_3$	$(CH_3)_3COLi/Nb(OC_2H_5)_5$	220	ND	Discharge capacity are lower than 100 mAh g^{-1} at 1 C	Discharge capacity can reach 116 mAh g^{-1} at 1 C	[73]
	$LiCoO_2/Li_{10}GeP_2S_{12}$	$LiNbO_3$	$(CH_3)_3COLi/Nb(OC_2H_5)_5$	235	1.8	Initial discharge capacity of 8.8 mAh g^{-1} and initial CE is 21.9%	Initial discharge capacity of 125.8 mAh g^{-1} and initial CE is 90.4%	[74]
	$LiCoO_2/Li_{10}GeP_2S_{12}$	Li_3NbO_4	$(CH_3)_3COLi/Nb(OC_2H_5)_5$	200	1	Retaining 66 mAh g^{-1} after 70 cycles	Retaining 118 mAh g^{-1} after 70 cycles	[75]
	$LiNi_{0.8}Mn_{0.1}Co_{0.1}O_2/SPE$	Li-Nb-O	$(CH_3)_3COLi/Nb(OC_2H_5)_5$	235	1.8	Capacity retention of 36.1% after 50 cycles	Capacity retention of 84.1% after 50 cycles	[76]
	$LiNi_{0.5}Mn_{0.2}Co_{0.3}O_2/ipn-PEA$	Li_3PO_4	$(CH_3)_3COLi/(CH_3O)_3PO$	250	0.6	The reversible discharge capacities are 136.9 mAh g^{-1}	The reversible discharge capacities are 179.9 mAh g^{-1}	[16]
	$LiNi_{0.8}Mn_{0.1}Co_{0.1}O_2/Li_{10}GeP_2S_{12}$	Li_3PO_4	$(CH_3)_3COLi/(CH_3O)_3PO$	250	ND	Completely failed after 50th cycle	133 mAh g^{-1} after 100th cycle	[77]
	$LiCoO_2/Li_6PS_5Cl$	Li_2ZrO_3	$[(CH_3)_2N]_4Zr/(CH_3)_3COLi/H_2O$	270	0.2	Retention of 48% after the 50th cycle	Retention of 72% after the 100th cycle	[78]

TABLE 2 (Continued)

Method	Electrode/SSEs	Layer materials	Precursor	Temp. (°C)	GPC (Å)	Electrochemical performance before	Electrochemical performance after	References
	Graphite/LiNi$_{0.5}$Mn$_{0.3}$Co$_{0.2}$O$_2$	Li$_3$BO$_3$-Li$_2$CO$_3$	(CH$_3$)$_3$COLi/[(CH$_3$)$_2$CHO]$_3$B/O$_3$	200	0.8	Capacity retention of 67.3% after 50 cycles	Capacity retention of 89.5% after 50 cycles	79
	LiNi$_{0.85}$Mn$_{0.05}$Co$_{0.1}$O$_2$/Li$_6$PS$_5$Cl	ZrO$_2$	Zr[N(CH$_2$CH$_3$)(CH$_3$)]$_4$/O$_3$	250	2.1	Capacity retention of 67.9% after 200 cycles	Capacity retention of 77.6% after 200 cycles	80
	LiFePO$_4$/Li$_{1.5}$Al$_{0.5}$Ge$_{1.5}$(PO$_4$)$_3$	ZrO$_2$	[(CH$_3$)$_2$N]$_4$Zr/H$_2$O	200	1.5	Average CE is 80%	Average CE great than 95%	81
	Li/Li$_7$La$_3$Zr$_2$O$_{12}$	ZnO	(C$_2$H$_5$)$_2$Zn/H$_2$O	150	2	1900 Ω·cm^2 (interfacial area specific resistance)	100 Ω·cm^2 (interfacial area specific resistance)	19
	LiNi$_{0.85}$Co$_{0.10}$Mn$_{0.05}$O$_2$/Li$_6$PS$_5$Cl	HfO$_2$	Hf[N(CH$_2$CH$_3$)(CH$_3$)]$_4$/O$_3$	250	1.5	Retention of 76% after the 60th cycle	Retention of 82% after the 60th cycle	82
	Li/Li$_{6.5}$La$_3$Zr$_{1.5}$Ta$_{0.5}$O$_{12}$	h-BN	B(N(CH$_3$)$_2$)$_3$/NH$_3$	450	2.8	Noisy signal with large polarization	Overpotential less than 12 mV after 400 h	21
MLD	LiNi$_{0.8}$Mn$_{0.1}$Co$_{0.1}$O$_2$/Li$_{10}$GeP$_2$S$_{12}$	PEDOT	MoCl$_5$/EDOT (C$_6$H$_6$O$_2$S)	150	5	Discharge capacity of about 10 mAh g^{-1} at 1 C	Discharge capacity is over 100 mAh g^{-1} at 1 C	83
	Li/Li$_{10}$SnP$_2$S$_{12}$	Alucone	TMA/(CH$_2$OH)$_2$	85	0.3	Short circuit after 4000 min	Overpotential less than 0.5 V within 10 000 min	84
	Na/Na$_3$SbS$_4$	Alucone	TMA/(CH$_2$OH)$_2$	85	1.5	Short circuit after 269 h	Overpotential is 0.45 V after 475 h	85
	Pt/Li$_{1.5}$C$_2$O$_{1.8}$	Li$_{1.5}$C$_2$O$_{1.8}$	(CH$_3$)$_3$COLi/(CH$_2$OH)$_2$	135	2.6	ND	Ionic conductivity with a value of 5×10^{-8} S cm^{-1} at 30°C	86
	Li/Li$_2$C$_8$H$_4$O$_4$	Li$_2$C$_8$H$_4$O$_4$	Li(thd)/TPA	200	3	Bare battery fails completely	Over 50% of the initial capacity at ~20 C	87
	Li$_2$C$_8$H$_4$O$_4$/LiPON	Li$_2$Q-LiPON	LiHMDS/HQ/DEPA	200	3	The cells lasted only for about 20 cycles before a rapid loss of capacity	Retention of 74% after the 100th cycle	63

Note: Li(thd) (thd = 2,2,6,6-tetramethyl-3,5-heptanedionate); TPA = C$_6$H$_4$[B(OH)$_2$]$_2$; LiPON = lithium phosphorous oxynitride; Li$_2$Q = dilithium-1,4-benzenediolate; DEPA = H$_2$NP(O)(OC$_2$H$_5$)$_2$; HQ = C$_6$H$_4$(OH)$_2$; LiHMDS = [(CH$_3$)$_3$Si]$_2$NLi.

3.1 | Lithium dendrites

Monroe and Newman calculated the effect of volume mechanical force on the formation of Li dendrite at the Li/SSEs interface using linear elastic theory.[92] They concluded that the shear modulus of electrolyte is more than twice that of Li metal (≥2 × 3.4–4.25 GPa), which can theoretically prevent the propagation of Li dendrites in SSEs. However, it was found that although the modulus of ISEs met the Monroe-Newman shear modulus criterion, the nucleation and growth of Li dendrites were still observed in different types of ISEs in the subsequent study, which showed that the propagation of Li dendrites depended on the integrity of Li/electrolyte
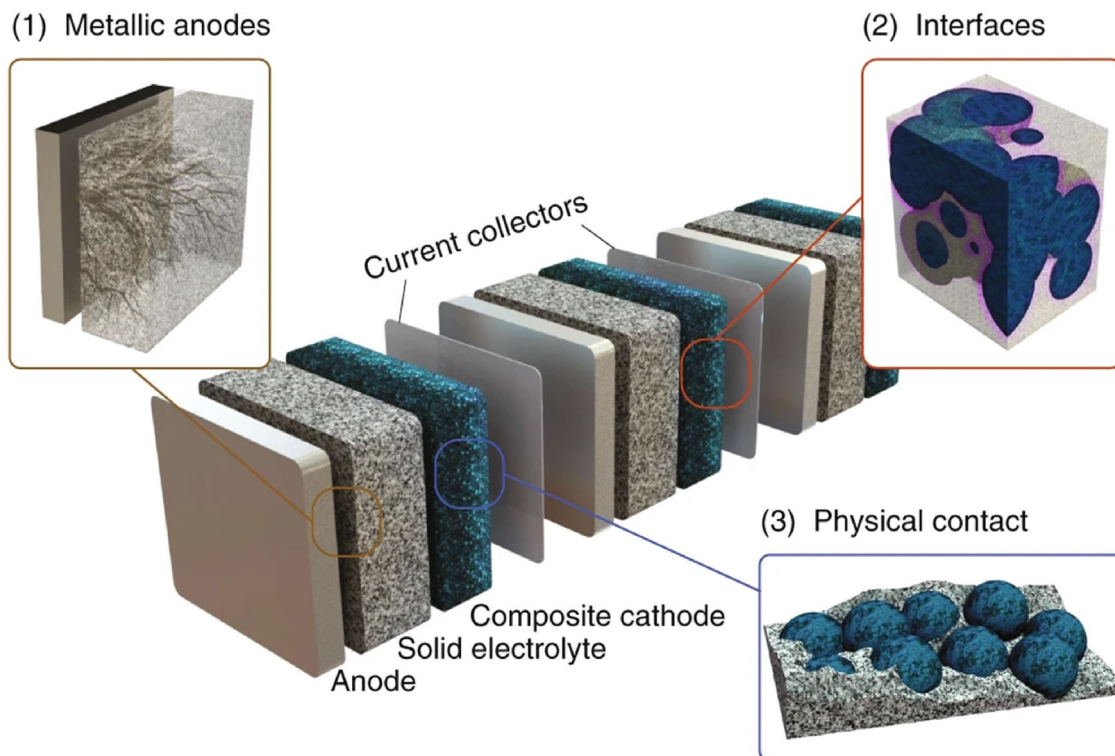
FIGURE 3 Schematic representation of main challenges of electrolyte and electrode interface. Reproduced with permission.[9] Copyright 2019, Springer Nature.

interface, not just the modulus characteristics of ISEs (Figure 4).[93–96]

In the process of gradually deepening the exploration of Li dendrites in ISEs, the researchers put forward a series of meaningful models for the growth mechanism of Li dendrites, which can be summarized into two categories. The first is the (metal Li) crystal growth model: dendrites grow along the grain boundary, and finally make Li dendrites penetrate the battery, causing the problem of short circuits. The second is the random electron reduction model: more precipitation points connected with each other, causing the problem of short circuits.

3.1.1 | Grain boundary growth model

The optimized interface of Li|ISEs has good wettability at the initial stage, and will have a good two-dimensional interface. However, with the increase in the number of cycles, the interface will become more and more uneven, which will increase the local current density and cause Li dendrite problems. Especially under the condition of high current density charging/discharging, the issue of Li dendrite in ISEs will be particularly significant, but the growth mechanism of Li dendrite in ISEs is different

from that in liquid electrolytes.[98,99] The Li dendrite in the battery containing liquid electrolyte will penetrate the diaphragm and cause the battery to fail due to short circuit.[100,101] The Li dendrite in the battery containing SSEs nucleates at the tip of the interface and grows along the grain boundary of the SSEs, and then passes through the electrolyte to cause a short circuit. In the initial exploration, the most widely accepted model is that of Li dendrite growth at the grain boundary, proposed by Sakamoto et al. (Figure 5A,B).[102] As shown in Figure 5C,D, the dendrite network that can be clearly observed fills the grain boundary, which strongly confirms that the dendrite of polycrystalline LLZO grows at the grain boundary.

After that, Chiang et al. prepared single crystal LLZO. In the experiment, it was found that the single-crystal LLZO could still grow Li dendrites (Figure 5E). It indicated that the dendrite sites were related to the smoothness of the surface, that is, the scratch on the surface, which provided the nucleation sites for the growth of Li dendrites.[98] In the following work, Chiang et al. proposed that the growth of dendrites is influenced by the distribution of an electric field, further perfecting the previous statement.[103] Different electric field models, namely current distribution models, have been established for the symmetrical battery with different relative sizes of
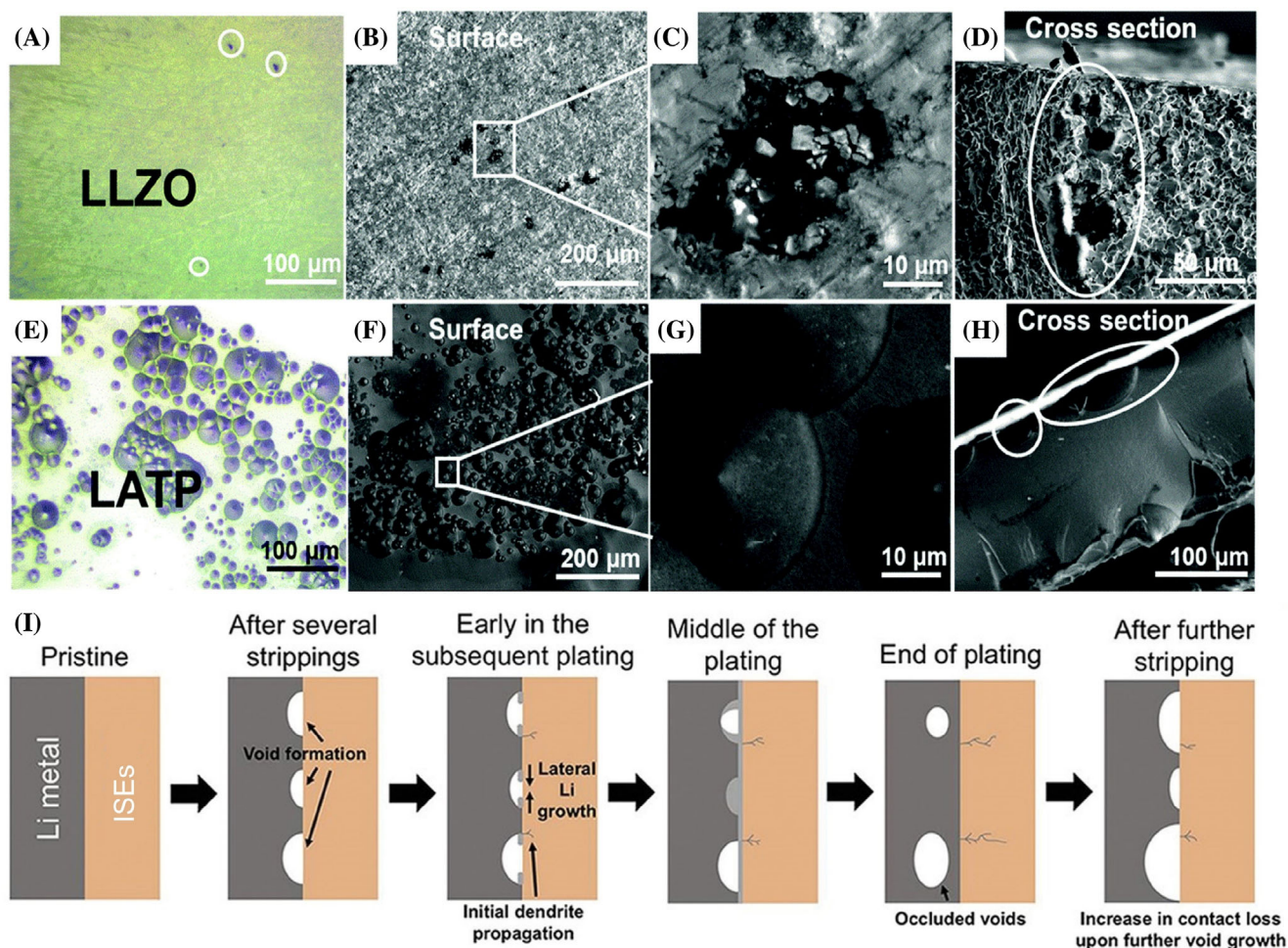
FIGURE 4 Morphologies of the surface and cross-section of (A–D) $Li_{6.1}Ga_{0.3}La_3Zr_2O_{12}$ (LLZO) and (E–H) NASICON-type Li_2O-Al_2O_3-P_2O_5-TiO_2-GeO_2 (LATP) after cycling. Reproduced with permission.[96] Copyright 2018, RSC Publishing. (A and E) Optical images of the surfaces of LLZO and LATP after cycling. (B and F) SEM of the surfaces and their enlarged areas of LLZO and LATP after cycling (C and G). (D and H) SEM of the cross sections of LLZO and LATP after cycling. (I) Schematic of Li metal/ISEs interface cycled at an overall current density. Reproduced with permission.[97] Copyright 2019, Springer Nature.

collector and Li. The results show that Li dendrites tend to grow at locations with relatively high current density, which is mainly due to the high local current density caused by poor contact.

3.1.2 | Electronic-conduction-induced model

Wang's group put forward different views based on the contradiction between dense LLZO (relative density > 97%) and grain boundary growth model and the effect of different surface scratch depths on dendritic growth, hoping to give a unified explanation for different experimental phenomena. Therefore, Wang et al. proposed that the dendritic growth was actually caused by the high electronic conductivity in the ISEs.[93] Because Li dendritic deposition only takes place in ISEs when two crucial criteria are satisfied, namely that the electrolyte must

contain mobile electrons (denoted by the electronic conductivity) and the potential of the electrolyte is lower than the Li electroplating potential (<0 V for Li/Li). The overpotential must provide sufficient driving force for the nucleation and growth of dendrites in ISEs. In addition, it was also observed that the amount of Li dendrite deposition detected with the increase of ambient temperature became more and more rapid. In the experiment, the growth process of Li dendrite at the interface between three ISEs with different electronic conductivity and Cu/Pt was observed by using in situ neutron depth profiling (NDP) technology (Figure 6). It found that Li did not show the sign of gradual growth from anode to cathode, but uniformly precipitated from the inside of ISEs. This statement has sparked considerable debate. The traditional Li growth mechanism suggests that Li dendrites are interconnected, leading to a reduction in Li quantity as the distance from the anode/electrolyte increases.
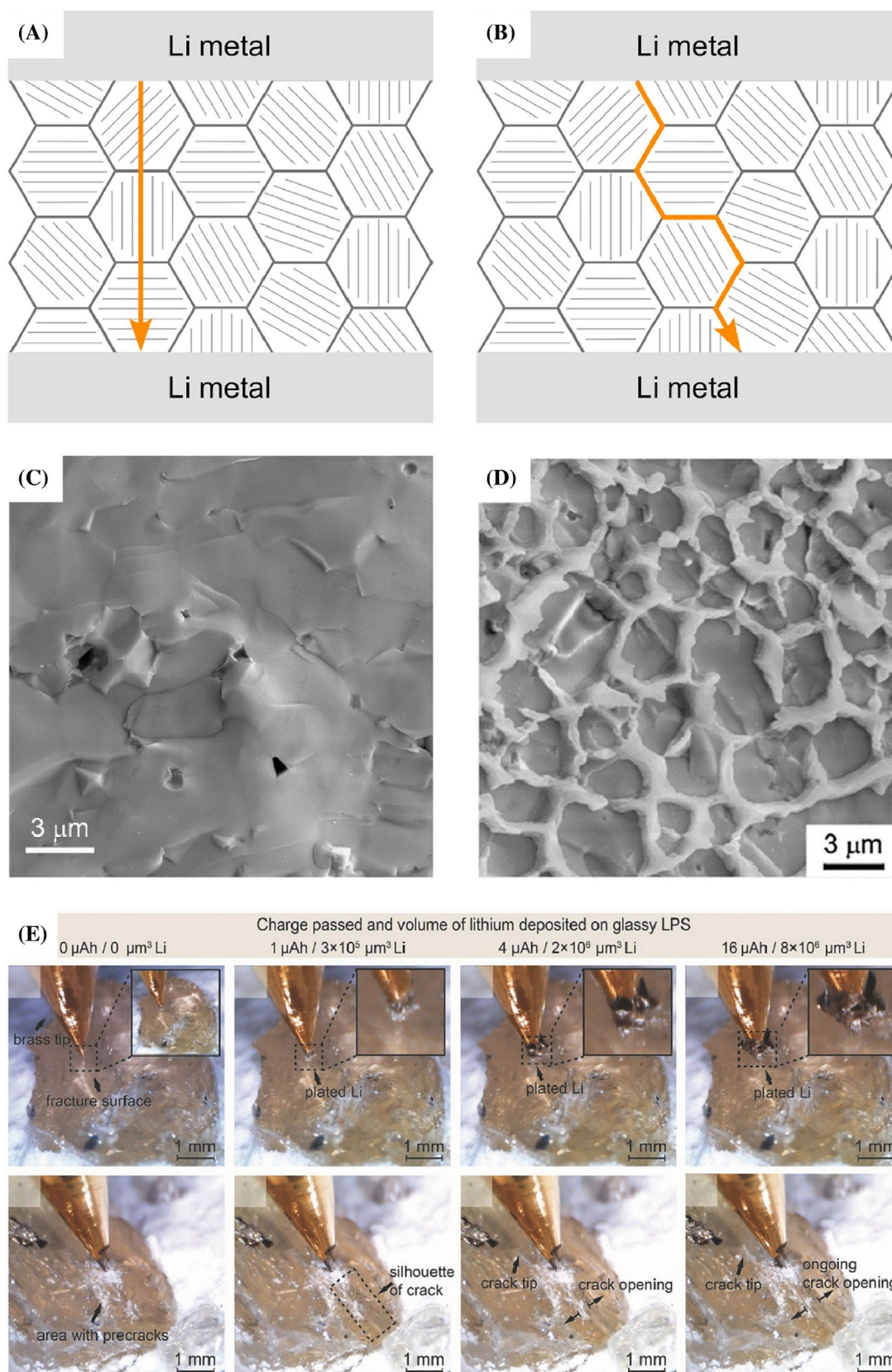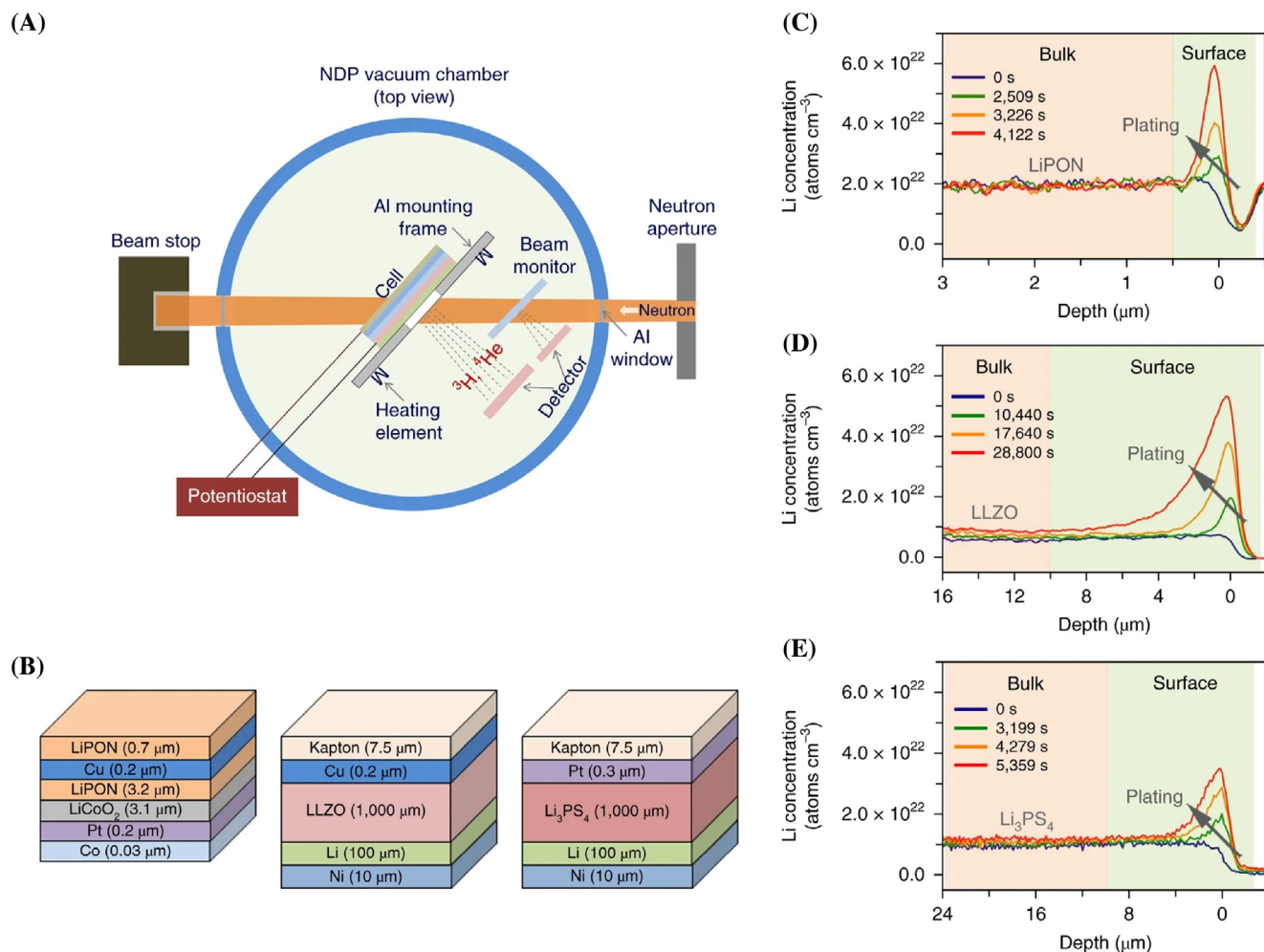
FIGURE 5 Legend on next page.

FIGURE 6 (A) Schematic diagram of the experimental setup for operating NDP. (B) Structural diagram of Cu/LiPON/LiCoO$_2$, Cu/LZO/Li, and Pt/Li$_3$PS$_4$/Li cells. Li is plated on Cu or Pt, and during plating, the depth distribution is determined from the cell's top surface. Time-resolved Li concentration profiles for (C) LiCoO$_2$/LiPON/Cu, (D) Li/LLZO/Cu, and (E) Pt/Li$_3$PS$_4$/Li cells. Cells examined at 100°C provided the Li concentration patterns in (D) and (E). The gray arrows represent Li's continuous plating. Reproduced with permission.[93] Copyright 2019, Springer Nature.

In contrast, Li deposition driven by electron conduction results in isolated dendrites, which do not exhibit sensitivity to the distance from the anode/electrolyte interface.

3.2 | Interface reactions

The composition and structural characteristics of the mesophase formed by the reaction between the electrode material and the electrolyte interface are of notable significance for Li$^+$ and electron transport at the interface, which determines the cycle stability of the IASSLBs. The chemical stability of the interface between the two is determined by the distribution of their intrinsic energy levels. If the lowest unoccupied molecular orbital (LUMO) of the electrolyte material is lower than the chemical potential of the negative material, and the highest occupied molecular orbital (HOMO) is higher

FIGURE 5 Diagram of Li metal plating through polycrystalline LLZO (A) transgranular, (B) intergranular. SEM image of (C) a fractured LLZO surface and (D) the web structure. Reproduced with permission.[102] Copyright 2017, Elsevier. (E) Optical microscope images captured during galvanostatic Li plating utilizing the brass electrode (10 mA cm^{-2} starting current density) at two separate locations on the surface of glass coated with Li$_2$S-P$_2$S$_5$ (LPS). The area of surface that the electrode tip came into touch with was devoid of any visible pores or fissures (the top four in the figure). An area that had been purposefully scratched with a tool with a diamond tip was in contact with the electrode tip (the bottom four of the figure). Reproduced with permission.[98] Copyright 2017, Wiley-VCH.
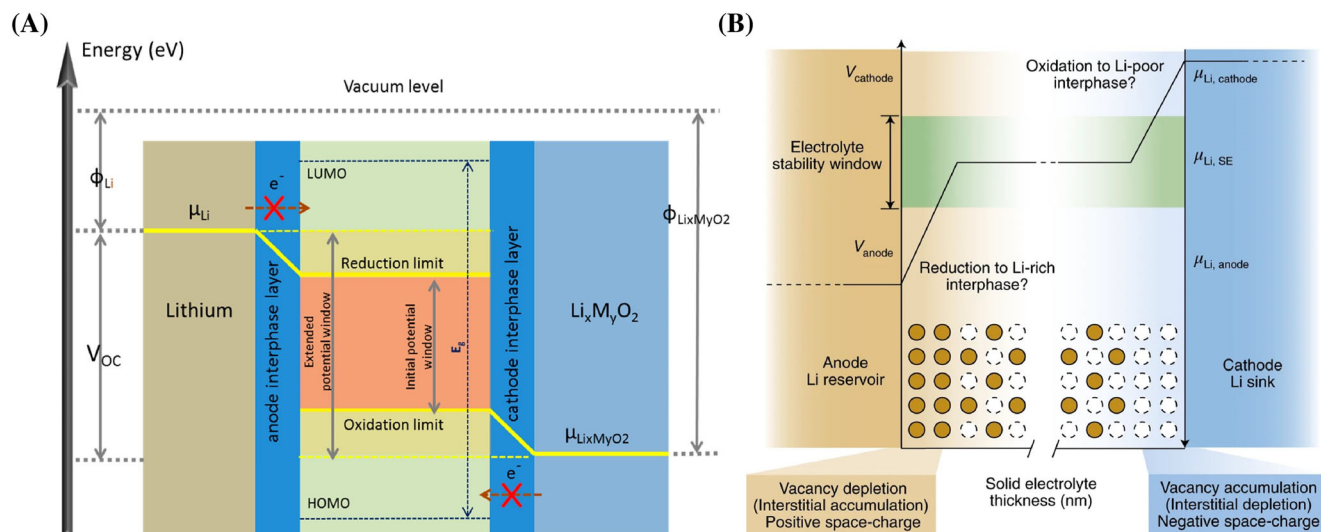
FIGURE 7 (A) Li-SSE-Li$_x$M$_y$O$_2$ solid-state battery system open-circuit energy diagram schematic illustration. Reproduced with permission.[104] Copyright 2019, American Chemical Society. (B) Chemical potential evolutions as the solid electrolyte in contact with the anode and the cathode. Reproduced with permission.[9] Copyright 2019, Springer Nature.

than the chemical potential of the positive material, a thermodynamic stable interface will be formed. In contrast, the interface reaction will occur, and the intermediate interface layer similar to the solid electrolyte interface (SEI) film in the liquid battery will be formed (Figure 7A).[4,104] The process formed by the chemically driven interface does not require external voltage. It can be viewed as a slow thermodynamic process dominated by chemical reactions. From the perspective of electrochemistry-dominated kinetics, whether the interface layer can be passivated to inhibit its rapid growth depends on the ionic conductivity and electronic conductivity of the interface reaction products (Figure 7B).[9,105]

3.2.1 | Chemical instability of Li/ISEs

The long-term stability of Li|ISEs interface is a necessary condition to ensure the performance of IASSLBs. However, once most SSE is contacted with Li metal electrode, especially those ISEs composed of sulfide and thiophosphate, are reduced at the interface to form SEI film. The existence of SEI and its properties have a wide influence on the Li-ion migration across the Li|ISEs interface. Researchers studying IASSLBs often encounter three distinct types of Li|ISEs interfaces: the dynamically stable Li|ISEs interface, the persistently reactive and unstable interface, and Li|ISEs interface with SEI generated by self-limiting reaction, as shown in Figure 8A–C.[106] For instance, the interface of Li|LLZO is dynamically stable; Li|Li$_{10}$GeP$_2$S$_{12}$ is a continuous reactive and unstable interface, resulting in an ionic and electronic mixed conductor;

Li|Li$_3$OCl is the interface that generates SEI through a self-limiting reaction.[88,107–110] Not long ago, T. McDowell et al. utilized in situ x-ray computed tomography to elucidate the progression of mechanical fracture damage in the form of black lines within Li$_{1+x}$Al$_x$Ge$_{2-x}$(PO$_4$)$_3$ (LAGP) SSE induced by interphase growth during constant current cycling in symmetric cells.[111] The cross-sectional image in Figure 8D reveals a strong contrast between the top and bottom surfaces of LAGP particles after cycling, which is attributed to the formation of reaction interface phases. In addition, the cross-sectional SEM image in Figure 8D shows a region of significant contrast at the top of LAGP particles that have cycled to failure. The expansion of this growth intermediate phase leads to stress and fracture in SSE. Figure 8E shows the relationship between the impedance of the battery and the total charge transferred during cycling, as well as the degree of fracture in the damaged area. The results indicate that as the cracks continue to grow, the transport of Li ions is hindered. Notably, this obstruction is not caused by the interface (which acts as a mixed ion-electron conductor), as the impedance does not significantly increase before crack initiation. In the data presented in Figure 8F,G, the damage near the edges of the particles is considerably less than that observed within the particles. This difference can be attributed to the fact that the Li metal anode interfaces only with 75% of the surface area of LAGP, leaving the outer edge untouched. This observation further suggests a correlation between the interactions at the Li-LAGP interface and the formation of cracks. Indeed, Li metal has demonstrated reduction capabilities across a wide range of known ISEs, including Ti-based Li$_{1.3}$Al$_{0.3}$Ti$_{1.7}$(PO$_4$)$_3$, Ge-based Li$_{1.5}$Al$_{0.5}$Ge$_{1.5}$(PO$_4$)$_3$,
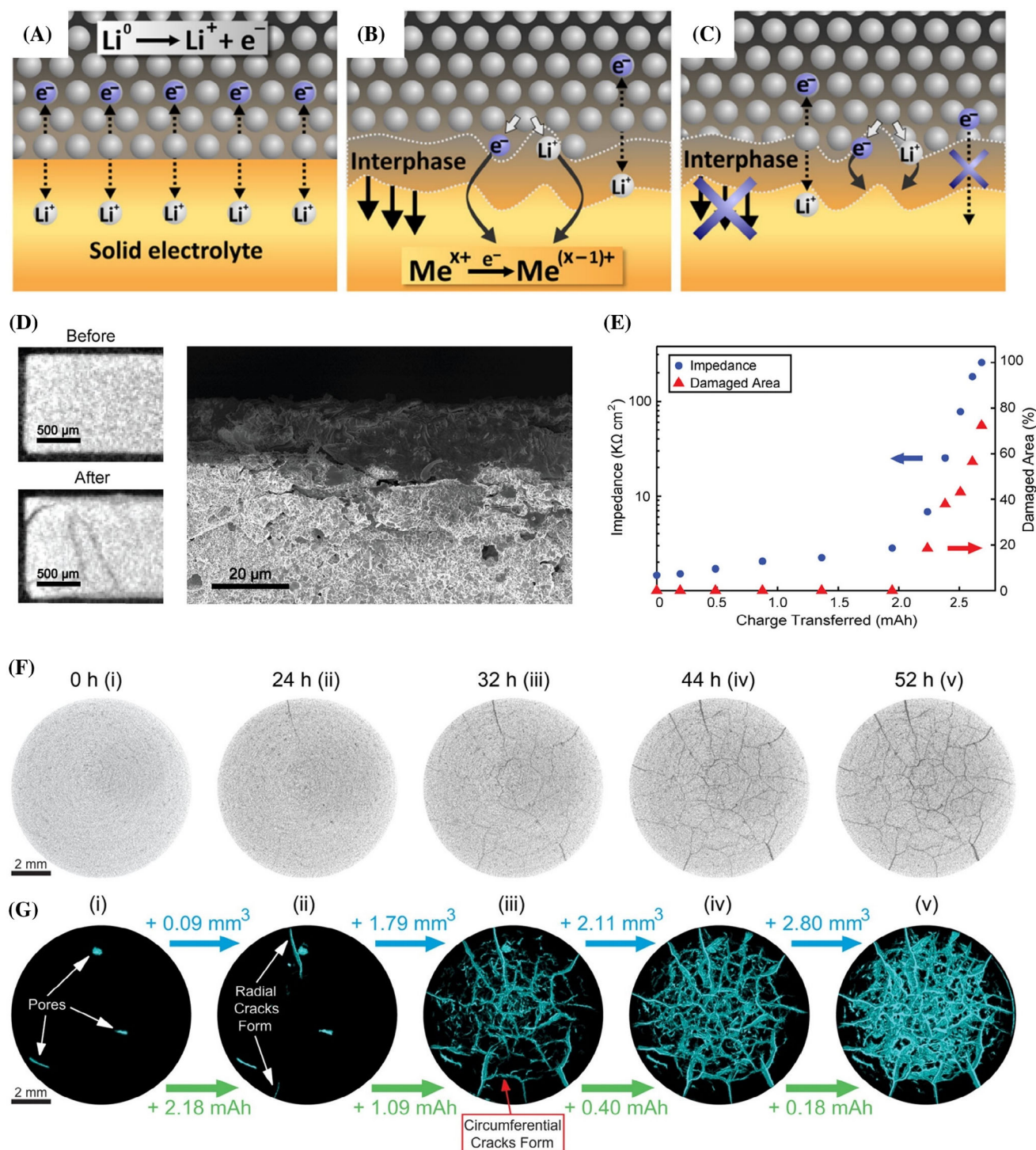
FIGURE 8 Schematic interface between Li metal and ISEs, (A) Stable interface, (B) continuous reaction and unstable interface produce mixed conductor SEI, (C) self-limiting reaction interacts with stable SEI. Reproduced with permission.[106] Copyright 2015, Elsevier. Interphase growth and fracture origin of $Li_{1+x}Al_xGe_{2-x}(PO_4)_3$ (LAGP). (D) Two-dimensional cross-sectional slices of LAGP particles before (top) and after (bottom) the cycle. After electrochemical treatment, a darker region is formed at the Li/LAGP interface, indicating that the interface region of the reaction is growing. And in situ cross-sectional SEM images of LAGP. (E) The impedance of different cells is plotted against the total amount of charge transferred. The effect of chemical instability of Li metal/ISEs interface on performance was observed by x-ray computed tomography scanning of LAGP|Li cell every 4 h. (F, G) 2D slices of LAGP particle centers extracted from 3D sectional images (i) before and after electrochemical cycling (ii) 24, (iii) 32, (iv) 44, and (v) 52 h. The black line indicates cracks in LAGP particles, forming a network pattern and the increase of crack volume is shown above the blue arrow, and the amount of transferred charge is shown below the green arrow. Reproduced with permission.[111] Copyright 2019, American Chemical Society.
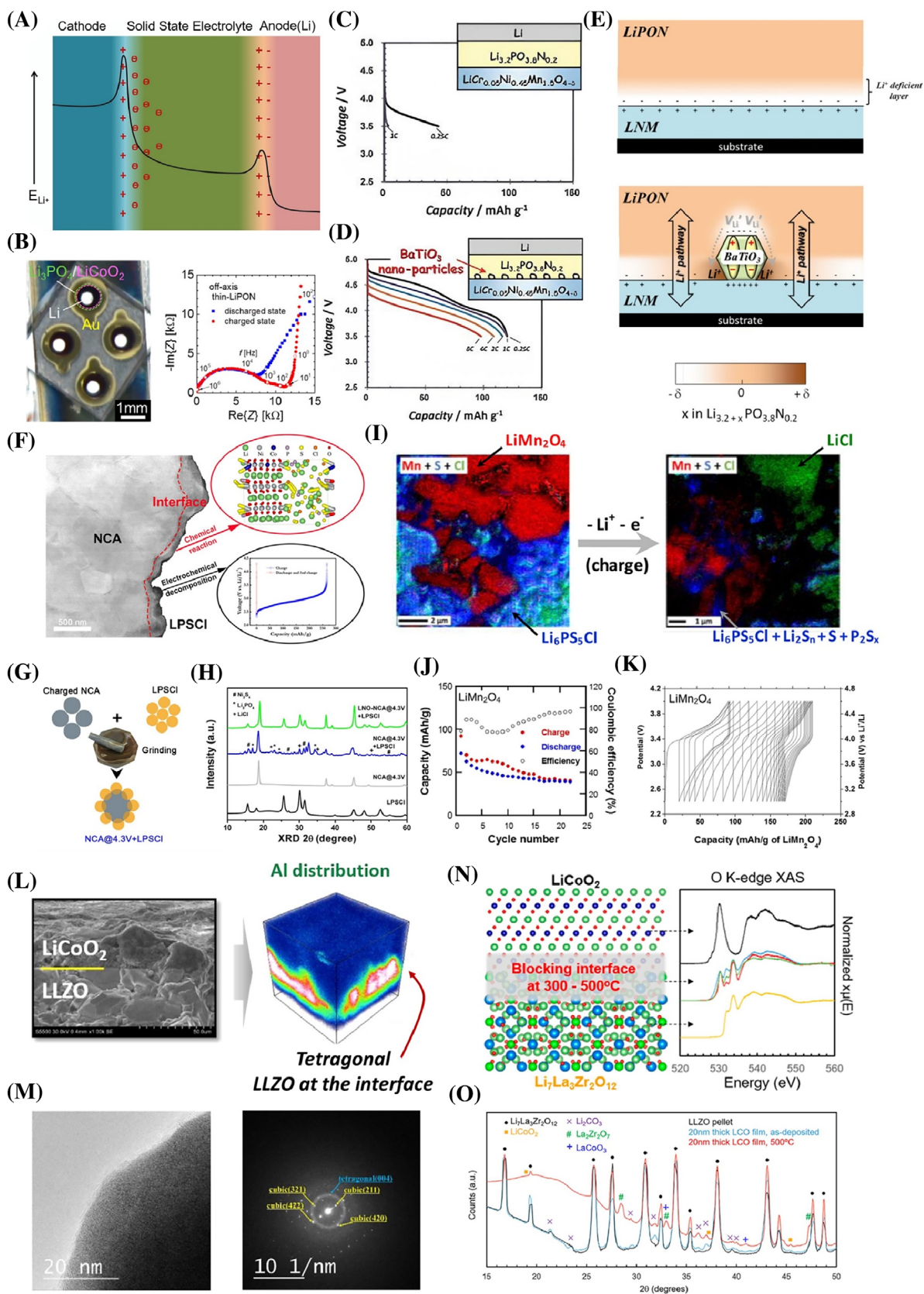
FIGURE 9 Legend on next page.

sulfide-based glass ceramics $Li_7P_3S_{11}$, and Li_4SnS_4.[112–114] The SEI film form under ideal conditions should be self-limiting, with good ionic conductivity and poor electronic conductivity. But this is not the case for the most part. Therefore, in order to obtain a stable Li|ISEs interface, it is also necessary to manufacture stable SEI manually or have one or more composite solid electrolytes that can react with Li to produce stable SEI components.

In addition to experimental research, theoretical calculation research can provide important experimental guidance for complex interface reactions. The interface characteristics of Li|Li_3PO_4 (LPO) and Li|Li_3PS_4 were calculated by Lepley and colleagues, who discovered that the former is stable while the latter is unstable.[115] Density functional theory (DFT) calculations by Chen and his colleagues revealed the equilibrium interface structure of Li|PS_4-$Li_{10}GeP_2S_{12}$ (PS$_4$-LGPS) and Li|GeS_4-LGPS [001], and they predicted that the two interfaces formed by SEI would result in interface instability and high interface resistance.[116]

3.2.2 | Interface incompatibility of cathode/ISEs

The interface incompatibility of the cathode includes many aspects, but the main ones are the space charge layer effect and the chemical stability between the cathode and ISEs. The space charge layer effect mainly occurs in the battery system with sulfide as the solid electrolyte (Figure 9A).[117] This effect occurs because of the change in the charge carrier concentration between the two phases.[118] First, the cathode material is generally a mixed conductor, while the solid electrolyte is a single ionic conductor. When the cathode is in contact with the ISEs, the large chemical potential difference between the two will cause the Li^+ to migrate to the anode side, and the concentration of the carrier will change and form a space charge layer. However, the cathode is an electronic conductor, so the electrons will be attracted by the space charge layer. The migrated electrons can just neutralize the Li^+ transferred to the cathode, and then the space charge layer on the side of the cathode disappears. However, the ISEs as a single conductor will seriously consume Li^+ near the side of the charge layer, so Li^+ in the ISEs will continuously move towards the side of the space charge layer to achieve electrochemical balance. The Li^+ concentration gradient in ISEs will be formed after the above process is repeated many times. ISEs, as electronic insulators, cannot offset this effect by the movement of electrons, which leads to the depletion of Li on one side of the ISEs and the sudden increase of interface resistance.[117,119,120] Haruta et al. deposited LiPON thin films using an off-axis sputtering configuration to address the negative space charge layer effect at the oxide electrolyte/electrode interface, and ultimately obtained an extremely low interface resistance of 8.6 Ω cm^2 (Figure 9B).[119] The results show that off-axis sputtering configuration can reduce interface sputtering damage, which reduces activation energy and achieves low interface resistance. In addition, a full vacuum manufacturing process should be used during the preparation process to prevent contamination at the electrolyte/electrode interface. Yada et al. deposited another layer of LiPON on the LNM cathode spin-coated with $BaTiO_3$ nanoparticles (BTN), and obtained that when discharged at 8 C rate, the battery still retained 84% (120 mAh g^{-1} at 0.25 C rate, Figure 9C,D).[120] This is mainly attributed to the fact that BTNs with larger dielectric constant can effectively suppress the charge transfer resistance at the LiPON/LNM interface ($R_{LiPON/LNM}$) (Figure 9E).

The oxidation potential of sulfide electrolyte is also low, and its irreversible oxidation process not only hinders the ion transmission and increases the charge

FIGURE 9 (A) The presence of a space charge layer at the electrode/ISEs interface is depicted schematically, with the black curve indicating the uneven electrochemical potential of Li^+ during charging. Reproduced with permission.[117] Copyright 2018, Elsevier. (B) Microscope image of a fabricated thin-film battery, alongside the impedance spectra of batteries featuring 100 nm thick LiPON deposited off-axis. Reproduced with permission.[119] Copyright 2015, American Chemical Society. The rate capabilities of an unmodified battery (C) are compared to those of a Li/LiPON/LNM battery (D) modified with BTNs, where the BTN layer is 100 nm thick. (E) Schematic photographs of the Li^+ concentration profile at a LiPON/LNM interface without modified and a BTN-modified LiPON/LNM interface during open-circuit circumstances. Reproduced with permission.[120] Copyright 2014, Wiley-VCH. (F) Cathodic interface reaction and electrolyte electrochemical decomposition phenomenon between LPSCl and high voltage cathode NCA. (G) Sample combination preparation for XRD is shown schematically. (H) XRD images of each combination at various charge states. Reproduced with permission.[122] Copyright 2019, American Chemical Society. (I) Before and after cycling, SAM mapping of Mn, S, and Cl elements in the composite LMO electrode from LMO/LPSCl/Li-In half-cells. Capacity retention, cycling efficiency behavior (J) and voltage profiles (K) for charge–discharge of LMO/LPSCl/Li-In half-cells. Reproduced with permission.[124] Copyright 2017, American Chemical Society. (L) Three-dimensional elemental photographs of the $LiCoO_2$/LLZO interface, enabled by TOF-SIMS, are shown in the inset SEM image. (M) TEM images and electron diffraction patterns of LLZO within $LiCoO_2$/LLZO. Reproduced with permission.[125] Copyright 2016, American Chemical Society. (N) O K-edge x-ray absorption spectroscopy (XAS) data (partial fluorescence yield mode). (O) Synchrotron XRD spectra for the LLZO pellet with a 20 nm LCO layer on LLZO, both in the as-deposited condition and after annealing at 500°C.[126] Copyright 2018, American Chemical Society.

transfer impedance, but also leads to the low CE of the first cycle of IASSLBs, thus affecting the cycle life of the battery. Koerver et al. observed a shift in the peak of the S 2p signal to higher binding energies as the charging cut-off voltage increased during their XPS characterization of the interface between NCM811 and sulfide electrolyte. This shift indicated that the electrochemical decomposition of electrolyte increased with the increase of voltage, which also accompanied the gradual increase of the mid-frequency semicircle attributed to the positive electrode/electrolyte interface in the Nyquist diagram.[121] The decomposition products gradually decrease with the increase of etching depth, indicating that the electrolyte decomposition near the collector is more serious. Banerjee et al. physically mixed the $LiNi_{0.85}Co_{0.1}Al_{0.05}O_2$ (NCA) with Li_6PS_5Cl (LPSCl) and charged it to 4.3 V (Figure 9F,G).[122] X-ray diffraction (XRD) characterization showed that even the original NCA mixed with electrolyte would produce LPO and Ni_3S_4, while the NCA charged to 4.3 V would react with Li_6PS_5Cl seriously to produce LPO, Ni_3S_4 and LiCl. Ni_3S_4 has electronic conductivity, which will make the interfacial reaction between them continue (Figure 9H). Zhang et al. also used x-ray photoelectron spectroscopy (XPS) to detect SO_x and GeO_2 in the composite positive electrode containing $LiCoO_2$, $Li_{10}GeP_2S_{12}$, and C65 (conductive carbon black) after cycling.[123] Besides, The interfacial interaction between Li_6PS_5Cl and $LiCoO_2$, $LiNi_{1/3}Co_{1/3}Mn_{1/3}O_2$, and $LiMn_2O_4$ (LMO) was studied by Auvergniot et al. using XPS and a scanning Auger electron microscope (SAM, Figure 9I–K).[124] The results showed a trend in the reactivity of Li_6PS_5Cl towards the three active substances, with the order of increasing reactivity observed as follows: $LiCoO_2$ < $LiNi_{1/3}Co_{1/3}Mn_{1/3}O_2$ << $LiMn_2O_4$.

In addition to the space charge effect commonly observed in sulfide solid electrolytes, the issues caused by the chemical instability of the interface cannot be ignored for IASSLB systems. Woo et al. used $LiCoO_2$ as cathode and sulfide as ISEs to form IASSLBs.[67] It was found that cobalt element would diffuse to the side of ISEs due to the electrochemical potential difference between the cathode and ISEs, and a cobalt sulfide layer approximately 30 nm thick was formed on the interface after using high-resolution transmission and energy spectrum analysis. In addition, the difference in chemical composition of S and O anions would cause incompatibility between the two phases. Park et al. co-sintered LLZO and $LiCoO_2$ at 700°C to achieve a close contact between LLZO electrolyte and $LiCoO_2$ and found that the transformation of $Li_7La_3Zr_2O_{12}$ from cubic phase to tetragonal phase along with the formation of La_2Co_4—Li ion insulating diffusion phase (Figure 9L,M).[125] Vardar et al. found that this diffusion phase can be formed at 300°C–

500°C, which leads to deterioration of electrochemical performance (Figure 9N,O).[126]

3.3 | Interfacial contact

In conventional liquid LIBs, the liquid electrolyte could penetrate into the pores of porous electrodes to form continuous interface contact with electrode materials due to their fluidity and good wettability. Even during battery charging and discharging, the electrode material undergoes volume expansion/contraction due to insertion/removal of Li ions, but this does not affect the electrolyte's ability to maintain adhesion to electrode particles with constant volume changes, which ensures good ion contact. Additionally, this electrochemical strain may result in hydrostatic pressure, an even force, in the liquid electrolyte. Yet, ISEs cannot "automatically" fill the void in IASSLBs. The interface between the two is usually a rigid contact attributed to the fact that both the electrode material and the solid electrolyte are hard and their particle surfaces are not completely smooth, which reduces the effective contact area between the active material particles and the electrolyte, raises interfacial impedance, and the depletion in battery capacity.[127,128] As shown in Figure 10, repeated volume changes of cathode particles during lithium insertion/removal can result in loss of contact at the interface and severely impede Li-ion transport. This occurs despite the application of mechanical stress intended to deform the solid material for better face-to-face contact.[129–131]

3.3.1 | Interfacial wettability

The poor wettability of the ISE surface to the Li metal makes it impossible for the two to contact closely. Point-to-point physical contact can seriously affect the transmission efficiency of Li^+ at the interface, making it hard to construct a relatively perfect interface and causing the initial resistance of the battery to be large. Most ISEs rely on physical external pressure for their contact with metallic Li, which has a high interfacial resistance. Some researchers have proposed using molten metal Li to contact ISEs to improve wettability, but the expected results have not been achieved. Most ISEs in contact with molten Li can directly induce strong chemical reactions, even if the melting point of the Li metal is only 180.5°C, direct contact of the LATP electrolyte with molten Li can even cause a fire.[133,134] Recently, it has also been found that Li_2CO_3 on the surface of LLZO is the root cause of non-infiltration (Figure 11A).[135] Sharafi et al. also found that LLZO containing Li_2CO_3 on the surface has a wetting
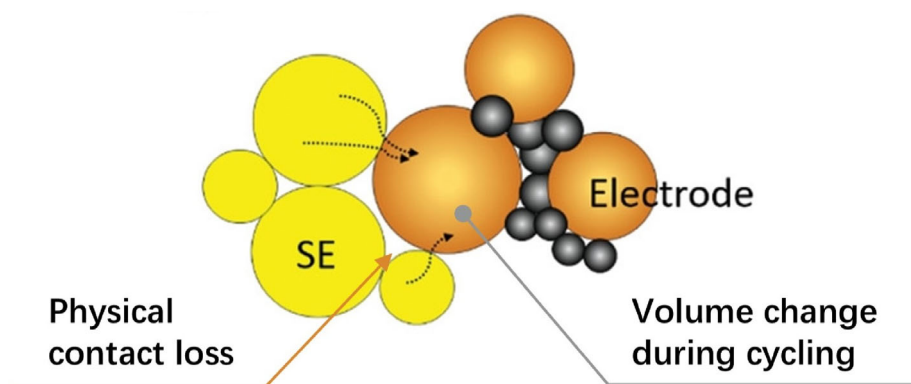
FIGURE 10 Illustration of the interfacial contact of the solid-state composite cathode. Reproduced with permission.[132] Copyright 2016, Springer Nature.

angle of 146° for Li metal, while polishing off Li_2CO_3 can achieve a wetting angle of 95° (Figure 11B).[136] After that, $Li_7La_{2.75}Ca_{0.25}Zr_{1.75}Nb_{0.25}O_{12}$ (LLCZN) materials, which are relatively stable for metallic Li, have the problem of not wetting molten Li, resulting in a large interfacial resistance at the interface (Figure 11C).[18] In recent years, many negative electrode materials have been reported on modifying the interface of lithiophilic layers to increase the wettability of molten Li on the electrolyte, and have strong affinity with the electrolyte, including Au, Ag, Si, Ge, Sn, ZnO, and other modified layers, as well as Li-Al, Li-C and other negative electrode materials with strong affinity with the surface of LLZO (Figure 11D,E).[19,137–145] Nevertheless, even if such materials enhance the wettability of the negative electrode, this will increase the risk of vertical growth of Li dendrites due to the reduction in surface energy. The same is true for the positive electrode/ISE interface, because the intrinsic characteristics of solids determine that solid electrolytes have relatively poor permeability and wetting ability for porous electrodes. It is extraordinarily hard for highly viscous molten ISEs to penetrate into the nanopores of the cathode material even at high temperatures.[146] To improve their interfacial contact, solid cathode particles can also be sintered with ISE powder (typically ceramic electrolytes). However, the quality of this electrode/ISE interface can be significantly impacted by sintering parameters (such as temperature, sintering duration, and pressure).[132]

3.3.2 | Volumetric effect

During the process of Li intercalation/deintercalation of positive electrode active materials, their crystal cell parameters will inevitably shrink or expand, resulting in volume deformation of material particles. Especially in IASSLBs, the ISEs and electrode particles are in point-

to-point contact, which is more sensitive to the volume change of the electrode material.[125] There is a tendency to cause poor contact between electrode particles and between electrode particles and electrolyte, or stress accumulation that leads to mechanical performance failure of the electrolyte during cycling, leading to degradation of the electrochemical performance of the battery.[145] Such as Janek et al. in situ monitored the interface contact and internal pressure during the cycling process of IASSLBs (NCM811/β-Li_3PS_4/Li).[130] As shown in Figure 12A, the interface between NCM811 and β-Li_3PS_4 produce significant gaps after 50 cycles. Moreover, the pressure monitoring data in Figure 12B shows that the internal pressure increases/decreases as the battery is charged/discharged, and the degree of change varies with the depth of charging and discharging.[130] The corresponding battery's charge and discharge capacitance also decrease rapidly, indicating that the volume change of electrode materials during the cycle has an important impact on battery performance. Figure 12C exhibits the curvature of the electrolyte cross-section in an IASSLB ($LiCoO_2/Li_{10}GeP_2S_{12}$/In) after initial charging.[148] Commonly used cathode materials in IASSLBs include $LiCoO_2$ ($\Delta V = 5.56\%$), $LiMnO_2$ ($\Delta V = 3.78\%$), $LiNi_xCO_yMn_{1-x-y}O_2$ ($\Delta V = 6\%$), $LiFePO_4$ ($\Delta V = 6.80\%$), and other materials that exhibit significant volume deformation except for the "zero strain" material $Li_4Ti_5O_{12}$ ($\Delta V = 0.2\%$). This can lead to changes in the internal contact conditions and pressure strain of the IASSLBs. To further understand the mechanical properties of sulfide electrolyte IASSLBs, McGrogan et al. measured the Young's elastic modulus (E), hardness (H), and fracture toughness (KIC) of $LiCoO_2$, Li_2S-P_2S_5, and metallic Li, as shown in Figure 12D.[149] The results suggest that lower Young's modulus allows Li_2S-P_2S_5 to adapt to the contraction and expansion of the electrode during cycling, but terrible toughness can lead to brittle fracture under pretty low stress at the same time.
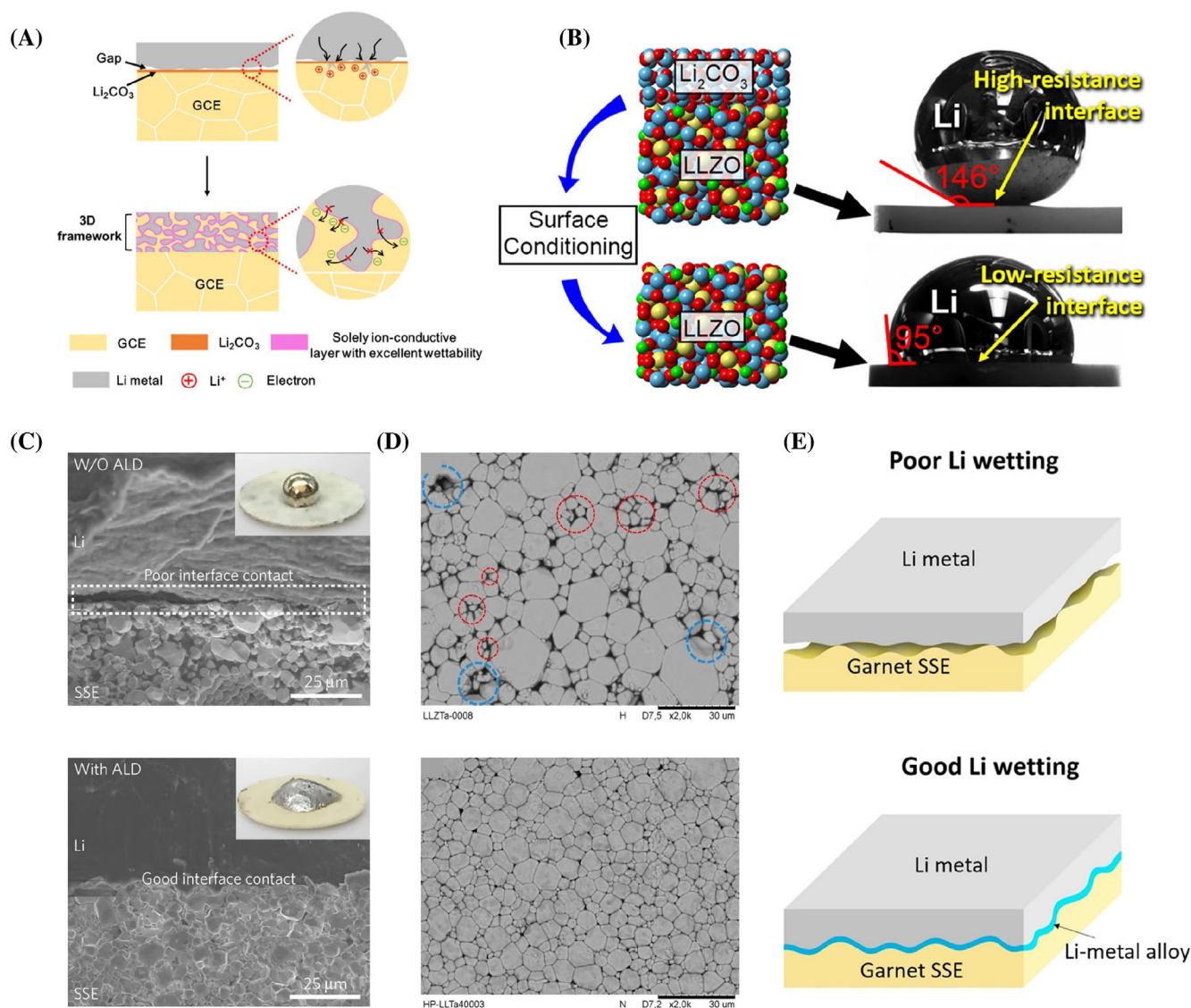
FIGURE 11 (A) Schematic of a superior garnet/Li interface for suppressing Li dendrites. Reproduced with permission.[135] Copyright 2020, American Chemical Society. (B) Contact angle measurements of liquid metallic Li after 500°C heat treatment on Li_2CO_3 and wet polishing on LLZO. Reproduced with permission.[136] Copyright 2017, American Chemical Society. (C) SEM diagrams of the interface between the Li metal and the garnet solid-state electrolyte. Reproduced with permission.[18] Copyright 2016, Springer Nature. (D) Microstructure of before and after hot-pressed. Reproduced with permission.[144] Copyright 2016, American Chemical Society. Closed porosity is indicated by the blue dashed circles, while the Al-Li glassy phase between the grains is indicated by the red dashed circles. (E) Diagram of the Li-metal alloy-based tailored garnet SSE/Li interface. Reproduced under the terms of the Creative Commons Attribution-NonCommercial license.[147] Copyright 2017, The Author, Published by American Association for the Advancement of Science.

Furthermore, Pervez et al. quantitatively analyzed the mechanical properties of ISEs through an electrochemical mechanical model.[150] It is stated that no fracture occurs when the ISEs meet the following conditions: Young's modulus is 15 GPa, fracture energy Gc $\geq$4.0 J m^{-2}, and total volume change of electrode particles ΔV $\leq$7.5%. Kasemchainan et al. studied the changes of metal Li of $Li/Li_6PS_5Cl/Li$ cells during charging and discharging through x-ray computed tomography (XCT) testing (Figure 12E,F).[97] It was found that a loose deposition layer would form on the surface of Li metal during

cycling, leading to severe volume changes in the negative electrode and interfacial separation from the electrolyte, which directly affected battery performance.

3.4 | ALD and MLD for interface design in IASSLBs

ALD and MLD technologies are increasingly recognized for their potential to overcome interface challenges in IASSLBs. These techniques offer precise
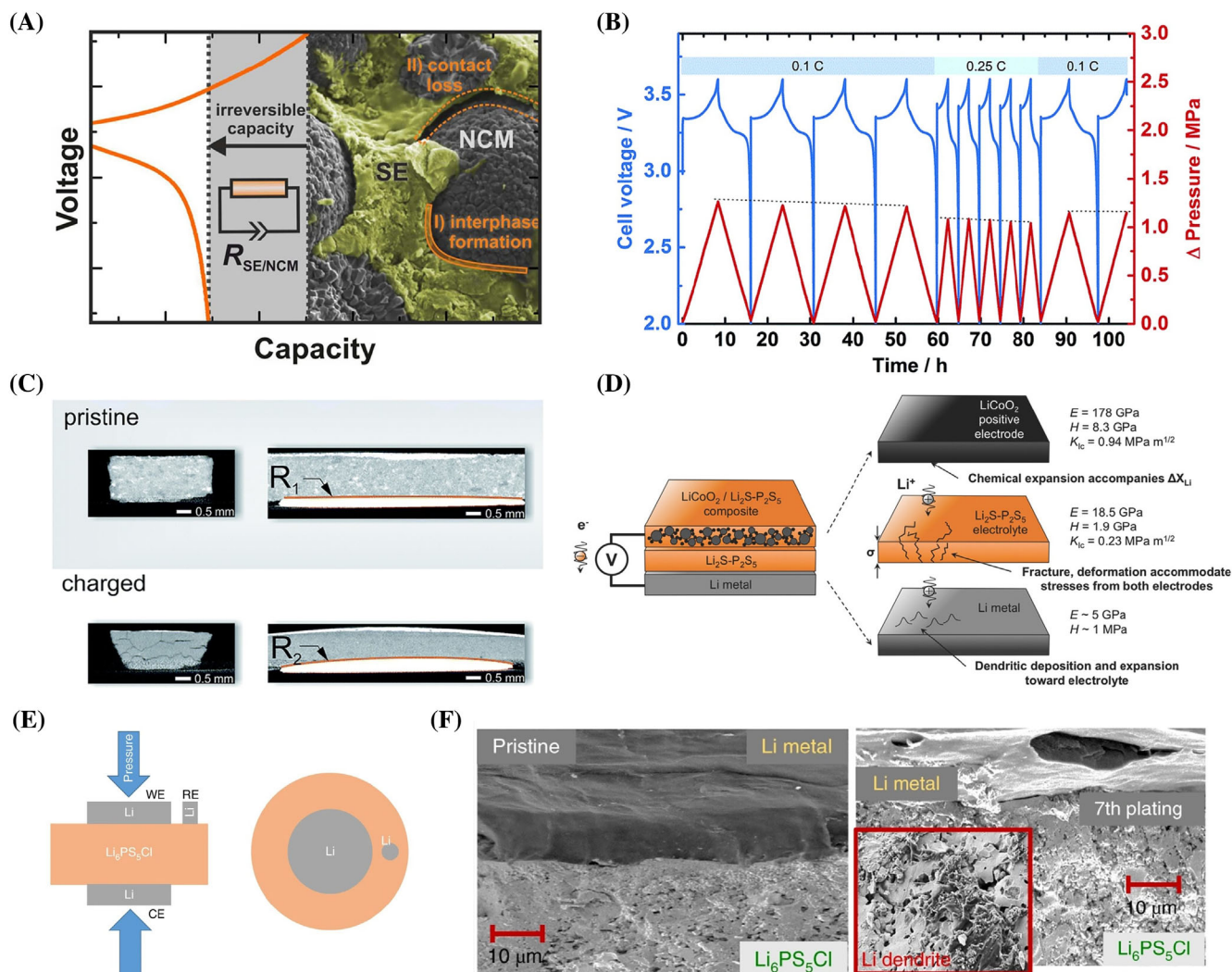
FIGURE 12 Volume effect of electrode interface. (A) illustration image of NCM811/β-Li$_3$PS$_4$/Li battery after cycling. Reproduced with permission.[130] Copyright 2017, American Chemical Society. (B) change of internal pressure in the battery of LiCoO$_2$/Li$_{10}$GeP$_2$S$_{12}$/In at different charging and discharging rates. (C) cross section x-ray tomography of LiCoO$_2$/Li$_{10}$GeP$_2$S$_{12}$/In battery before and after charging. Reproduced with permission.[148] Copyright 2017, Royal Society of Chemistry. (D) mechanical properties of LiCoO$_2$/Li$_2$S-P$_2$S$_5$/Li battery material. Reproduced with permission.[149,151] Copyright 2017, Wiley-VCH. (E) Three-electrode cell schematic. (F) SEM cross-sections of the Li metal/Li$_6$PS$_5$Cl interface. Reproduced with permission.[97] Copyright 2019, Springer Nature.

control over the deposition of thin films at the atomic level, which is crucial for addressing issues such as interfacial resistance and stability. By applying ALD and MLD, researchers can create conformal, uniform coatings on electrode materials and solid electrolytes, enhancing the mechanical and chemical compatibility between different layers. This results in improved ionic conductivity and a longer cycle life of the batteries. Moreover, the ability to tailor film thickness and composition at the nanoscale helps mitigate the effects of volume changes and interfacial degradation, thus advancing the overall performance and reliability of IASSLBs.

4 | INTERFACE PROTECTION MECHANISM

The use of ISEs in all IASSLBs can improve safety, and the ion conductivity of ISEs can be significantly improved by ameliorating preparation processes and elements doping. However, the interface impedance may be too large, hindering ion transport, and thus affecting battery performance due to electrolyte and electrode interface issues in the application of IASSLBs based on ISEs. An ideal ISE and electrode contact interface should have the following properties: firstly, it should have high ion conductivity; Secondly, outstanding interfacial wettability is required

to achieve a high contact area between solid and solid interfaces; Finally, the chemical stability of the interface in the charge–discharge process. To accomplish the above goals, introducing a modification layer into the interface using ALD/MLD is an effective approach for addressing the interface problems of the ISEs, alongside modifications to the solid electrolyte. For various situations, different modification layers can improve interface contact, inhibit the formation of Li dendrites, and reduce interface impedance. Due to its numerous advantages, ALD/MLD film formation technology is not only applicable in the field of Li batteries, but also in many industries such as catalysts, drug delivery, fuel cells, microelectronics, supercapacitors, semiconductors, and photovoltaics. In this context, we emphasize the critical importance of ALD/MLD for the next generation of IASSBs, and its potential applications in IASSLBs for future research.

4.1 | Passivation

The rate capability of most IASSLBs, especially those using high-voltage oxide cathodes, is still unsatisfactory.[152,153] This is usually attributed to the high internal resistance at the interface, but the exact fundamental physical and chemical mechanism of this resistance formation is indefinable to determine through experiments.

Battery performance problems can be brought on by mechanical problems, electrochemical reactions, and chemical incompatibility. Zhu et al. adopted density functional theory (DFT) to simulate the influence of coating materials, such as $Li_4Ti_5O_{12}$, $LiTaO_3$, $LiNbO_3$, Li_2SiO_3, and LPO, on the electrochemical stability of ISEs.[154] Based on the computed results, these coating materials exhibit an electrochemical window with a reduction potential ranging from 0.7 to 1.7 V and an oxidation potential from 3.7 to 4.2 V. Since the normal voltage range during the cycling of LIBs is between 2.0 and 4.0 V, this indicates that the coating material remains stable during the charging and discharging process. Considering the relatively poor electronic conductivity of the coating material, it can be used as an artificial SEI to passivate ISEs through the mechanism shown in Figure 13A. By decreasing the low Li chemical potential applied by the cathode material on the solid electrolyte material through the coating material, it is possible to extend the oxidation potential (anode limit) of the ISEs and suppress cathode interface oxidation and delithiation. This is particularly true for sulfide solid electrolyte materials, which are typically oxidized at a voltage as low as 2.0 V and thermally unstable at 4.0 V. Similarly, the above artificial coating strategy can also be applied to the anode side for reasons that protect and stabilize Li metal anodes. Richards et al.

employed DFT to check the bulk thermodynamics of various cathode and electrolyte configurations, including materials whose thermodynamic characteristics had not been established via experimentation (Figure 13B).[155] The calculation results show that stable electrolyte materials exhibit low reaction energy when in contact with the cathode and electrolyte. The application of the cathode lithium potential, as well as the powerful interaction between the PS_4 group and the oxide cathode to produce PO_4 groups and transition metal sulfides, are the main causes of the high reaction energy that is frequently present in thiophosphate materials. In contrast, the reaction energy between $LiAlO_2$ and LPO with the cathode is far less than that of thiophosphate materials regardless of combining with $LiCO_2$ or other oxide cathode materials. Nolan et al. performed a high-throughput thermodynamic analysis on the stability of LLZO garnet and high-energy NMC cathodes to determine potential coating materials in the same way.[156] Through evaluation of stability among binary oxides, lithium ternary oxides, lithium quaternary phosphates, borates, silicates, and ternary lithium halides with lithiated/delithiated NMC cathodes and LLZO, it was found that lithium ternary oxides generally exhibit superior stability compared to other chemical compounds when paired with LLZO. Higher Li content materials have lower decomposition energies in LLZO, as determined by calculation, but lower Li content materials are more stable in NMC, particularly in delithiated NMC or high voltage. This tendency may be explained by the fact that LLZO with a high Li content will only reach equilibrium Li chemical potential (μ_{Li}) when it comes into contact with compounds that have a high Li content and Li metal; as a result, the equilibrium Li chemical potential of LLZO and NMC is different. LLZO has a tendency to lithiate the material in touch if the contact material cannot establish equilibrium Li chemical potential, whereas NMC has a lower μ_{Li} and tends to absorb Li from sources rich in Li. Hence, these diversities in μ_{Li} between LLZO and cathode are the reason for their weak interface stability.[157,158] Further investigation showed that all layered oxide cathodes had comparable stability tendencies. Moreover, NMC111 is stable with Li_2O and $LiAlO_2$ in the decomposition energy of Li-Al-O ternary composition space, as well as all components along the connecting line (including Li_5AlO_4), which can be a stable coating choice for the cathode (Figure 13C). When compared to LLZO, the stability of the Li-M-O system with varied cationic M is noticeably different. Nb, $LiNbO_2$, $Li_8Nb_2O_9$, Li_2O, and Li_2O_2 are all stable with LLZO in the Li-Nb-O system, and any mixed components in this region are similarly stable with LLZO (Figure 13D). This indicates that the Li-M-O system with a large composition range
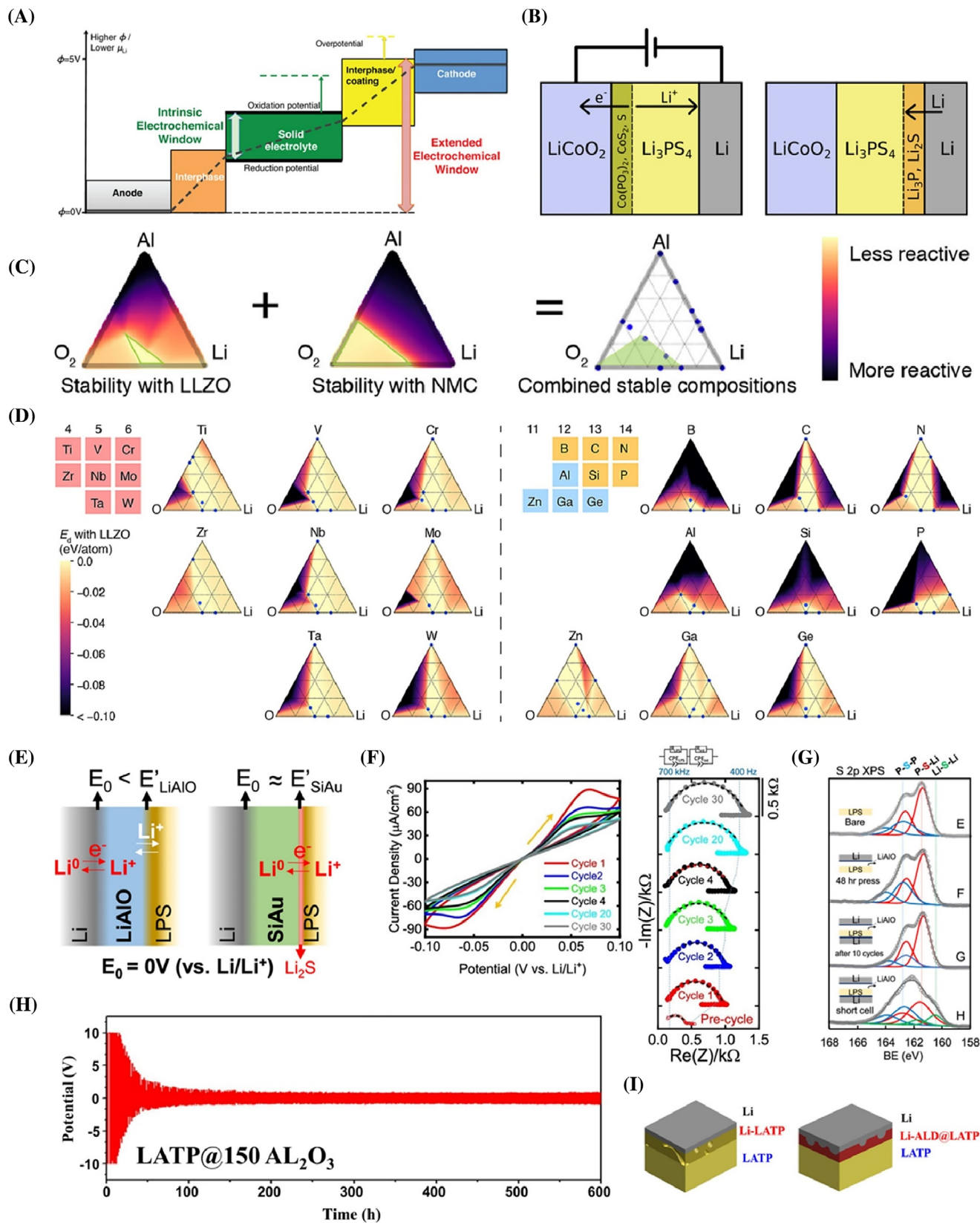
FIGURE 13 Legend on next page.

stable with LLZO is a promising coating material for LLZO. In terms of experiments, Sang et al. introduced a lithium conductive layer LiAlO at the $Li_7P_3S_{11}$ (LPS)/Li interface through ALD technology to diminish the potential between Li and LPS and defend ISEs from the effect of low potential, as shown in Figure 13E.[159] CV and impedance results reveal that the presence of LiAlO interlayer is able to stabilize ISEs and prevent the formation of Li dendrites due to cracks and decomposition (Figure 13F). The sulfur oxidation state in the S 2p XPS spectrum obtained from the LPS surface exhibits that the peak area ratio of sulfide (Li_2S) generated by the reduction of LPS with Li metal, represented by the low binding energy (near 160 eV) under the shielding of LiAlO interlayer, is dramatically declined (Figure 13G). This further demonstrates the capacity of LiAlO is isolate LPS from contact with Li and prevent LPS from being reduced to products with Li_2S on the surface of Li. In addition, Liu et al. established a multimodal characterization method to reveal that the ALD-Al_2O_3 coating mitigates the chemical deterioration of the Li metal/LATP interface by altering the evolution of SEI chemistry and morphology, leading to low overpotential for Li||Li symmetric batteries (Figure 13H,I).[68]

Sun's group has made astonished and effective progress in the interface electrochemical regulation of IASSLBs by ALD/MLD.[17,68,74,76–78,84,160] Such as a dynamic degradation surface passivation model with single crystal NCM523 as the target was established by in situ electrochemical atomic force microscopy (EC-AFM) technology and introducing LPO coating layer on the surface of single crystal nickel rich positive electrode via ALD (Figure 14A).[16] As shown in Figure 14B,C, the characterization of Aberration-corrected transmission electron microscopy (ACTEM) on the surface of single crystal NCM523 coated with a modified layer (L-NCM) shows that the LPO uniform coating with a thickness of approximately 5.28 ± 0.09 nm and the multilayer structure is unaffected by the coating procedure. The in situ EC-AFM

experiment showed that the uneven growth and distribution of the surface amorphous film (CEI) on the uncoated single crystal NCM523 (P-NCM) during the charging/discharging process give rise to significant fluctuations in the DMT (Derjaguin–Muller–Toporov) modulus (Figure 14C). However, L-NCM did not observe significant changes on the particle surface under the charging state, and the amorphous thin film grown during the process gradually diffused and homogenized, which is undoubtedly more outstanding compared to P-NCM (Figure 14D). Besides, P-NCM not only fails to grow uniform and dense CEI, but also causes the expansion of surface defects, component degradation, and the generation of irregular by-products (Figure 14E). At 0.1 C rate, the full battery's electrochemical performance revealed that L-NCM achieved a reversible discharge capacity of 179.9 mAh g^{-1} (with P-NCM at 136.9 mAh g^{-1}, Figure 14F). Even at a rate of 2.0 C, L-NCM maintains a stable reversible capacity of 102.1 mAh g^{-1}. Similarly, in the galvanostatic measurement at 0.2 C, LCM exhibited stable cycling, all attributed to the remarkable passivation effect of the stable and uniform LiF-rich CEI film on the interface of L-NCM cathode surface. Prior to this work, Tarascon et al. also adopted ALD-LPO and electro-analytical/spectroscopic techniques to conduct in-depth studies on the interface behavior between Ni-rich layered cathodes and halide-based SSEs.[161] As displayed in Figure 14G, $Li_{1.14}Mn_2O_4$:Li_3InCl_6:VGCF composite material mixture as a stable reference electrode to investigate the impact of parasitic redox processes on cell resistance. The changes in positive electrode impedance of three-electrode batteries held at voltages of 3.3, 3.6, and 3.9 V indicate that interface resistance increases rapidly within the first 10 h of voltage holding, followed by a slower rate of increase. The amplitude of this resistance follows the order of 3.9 V ≫ 3.6 V > 3.3 V (Figure 14H). This clearly indicates that a potential of 3.3 V is sufficient to trigger the parasitic redox process. To get a deeper insight into this parasitic reaction, the voltage holding time of the

FIGURE 13 (A) Diagrammatic representation of the electrochemical window (color bars) alongside the Li chemical potential profile (black line) for IASSLBs. Reproduced under the terms of the CC-BY Creative Commons Attribution 4.0 International license.[154] Copyright 2015, The Author, Published by American Chemical Society. (B) Decomposition/reduction of the electrolyte at the interface. Reproduced under the terms of the CC-BY Creative Commons Attribution 4.0 International license.[155] Copyright 2015, The Author, Published by American Chemical Society. (C) Heatmap of the decomposition energy of Li-Al-O compositions adopting NMC111/LLZO. (D) Chemical stability heatmaps for Li-M-O with LLZO (Ed = B, C, N, Al, etc.). Reproduced with permission.[156] Copyright 2021, Elsevier. (E) The electrochemical potential of LPS/SiAu and LPS/LiAlO is depicted in a cartoon. (F) The Li/LiAlO/LPS/LiAlO/Li cell underwent cyclic voltammetry (CV) at 0.2 mV/s. The corresponding Nyquist plot shows measurements taken before (red open circle) and after cyclic CV. (G) S 2p XPS spectra from a Li/LPS/Li symmetric cell with LiAlO interlayers. Reproduced with permission.[159] Copyright 2018, American Chemical Society. (H) Voltage characteristics observed during cycling of ALD-coated Li-Li symmetric cells. (I) Illustration showing the configuration differences between ALD-coated and uncoated Li-Li symmetric cells. Reproduced with permission.[68] Copyright 2018, American Chemical Society.
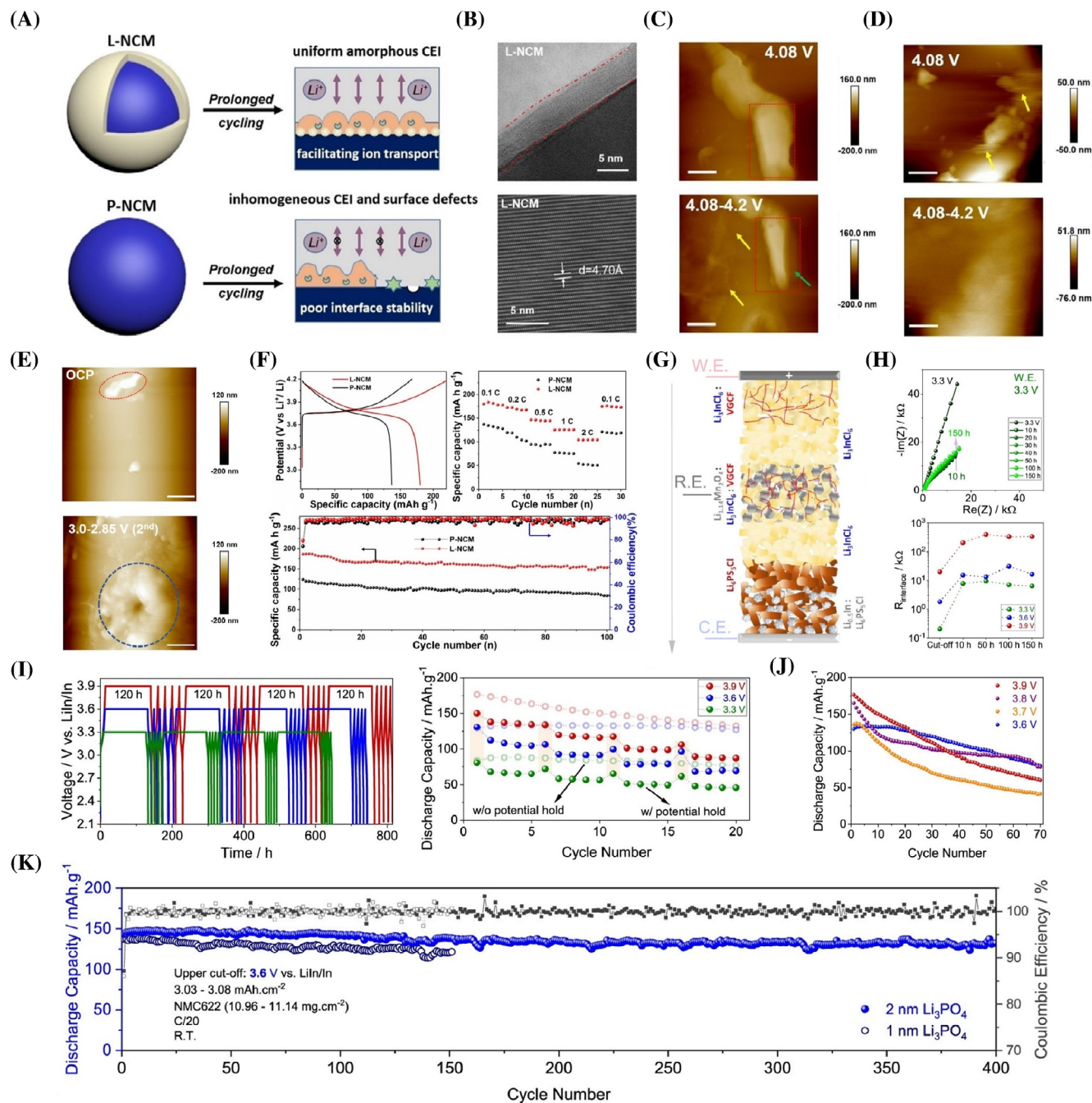
FIGURE 14 Volume effect of electrode interface. (A) Illustration image of the surface deterioration and interfacial regulation mechanism of the P-NCM and L-NCM electrodes. (B) The LPO coating layer on the surface of L-NCM is depicted in the ACTEM images. During charging at 4.08 V and 4.08–4.2 V, in situ AFM images depicting the topography on the P-NCM (C) or L-NCM (D) electrode surface. (E) The morphology of the production process of surface defects on the P-NCM cathode is captured by in situ AFM images. (F) Performances of P-NCM and L-NCM electrochemically in IASSLBs. Reproduced with permission.[16] Copyright 2022, Wiley-VCH. (G) Illustration of the three-electrode cell setup that measures impedance. (H) Working electrode impedance spectra were recorded at 3.3 V cut-off potentials and Plot, illustrating the evolution of modeled interfacial resistance as a function of voltage hold duration. (I) Constant voltage procedure during the aging process of the cell while cycling at various voltages and long-term cycling performance compare capacity retention to cells without voltage hold (shaded data). (J, K) Performances of containing or un-containing LPO coated electrochemically in IASSLBs. Reproduced with permission.[72] Copyright 2022, American Chemical Society.

additional three two-electrode cells, made of a hand-grinded NMC622/Li₃InCl₆/VGCF composite, was extended to 120 h, followed by four voltage-free

intercalation/de-intercalation cycles and the entire operation was repeated (Figure 14I). It is clearly observed from the retention rate of discharge capacity that the
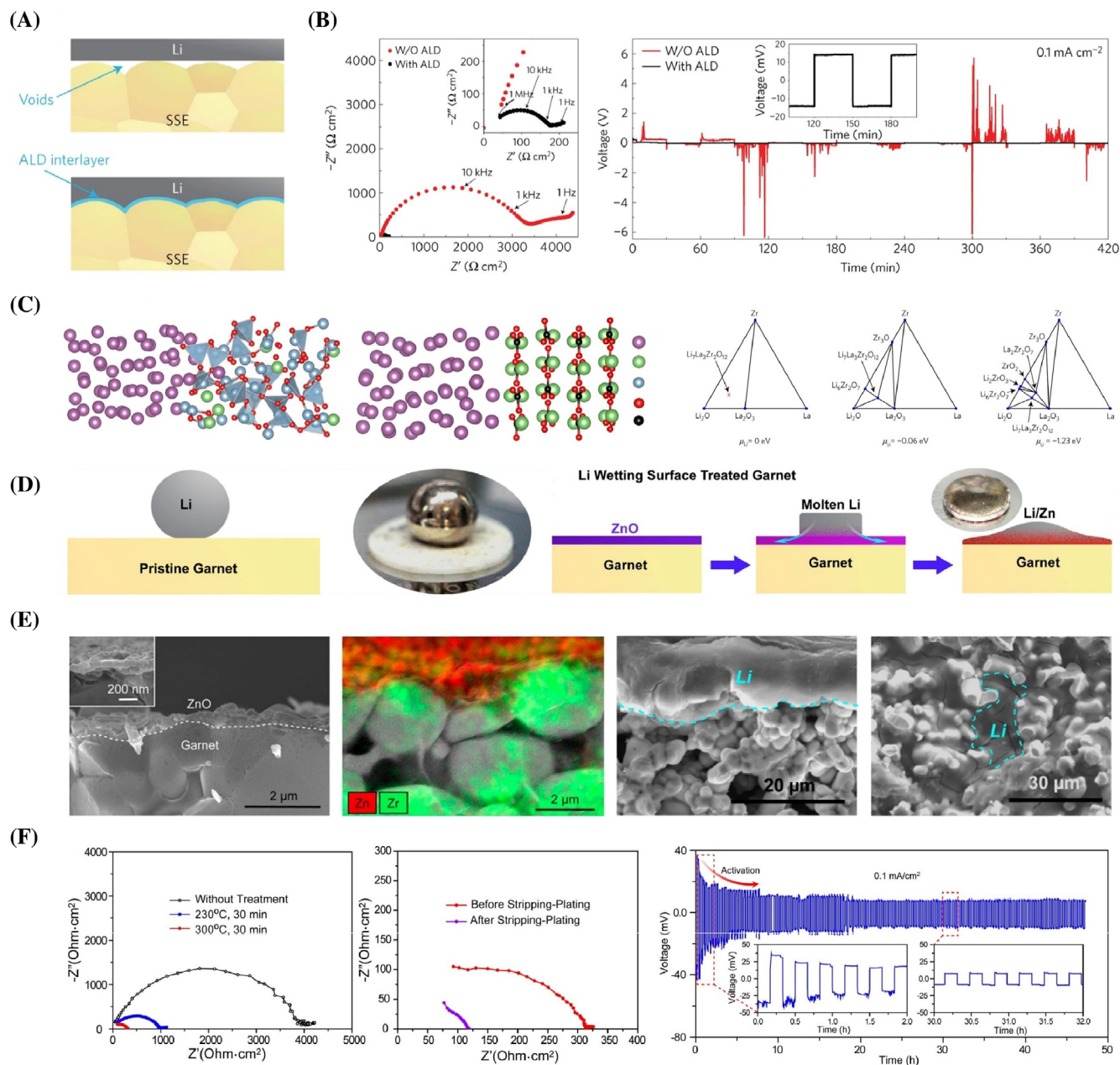
FIGURE 15 (A) Illustration diagram of the wetting behavior of molten Li on a garnet surface. (B) Comparison of Electrochemical impedance spectroscopy (EIS) profiles and cycling of the symmetric cells. (C) Interface models of $LiAl_5O_8$ and Li_2CO_3 from ab simulations, as well as Li grand potential phase diagrams showing the phase equilibria of an LLZO system. Reproduced with permission.[18] Copyright 2016, Springer Nature. (D) Illustration of molten Li wetting surface-treated garnet. (E) SEM photographs and elemental mapping of the ALD ZnO-coated garnet electrolyte, as well as cross-section SEM images of either Li-infiltrated porous garnet with ZnO surface treatment or Li-infiltrated porous garnet with a porosity of 60%–70%. (F) Electrochemical performances of Li/Garnet/Li symmetric cells. Reproduced with permission.[19] Copyright 2017, American Chemical Society.

irreversibility of cells cycling without voltage hold is lower, further confirming this time-dependent decomposition at high voltage (Figure 14J). It is also well consistent with the results disclosed by cycling stability performance that there is an electrochemical triggered decomposition reaction of ISE at high potential, which leads to a rapid decay of the discharge capacity of solid-state batteries from ~125 to ~80 mAh g^{-1} at a rate of C/20 after 70 cycles. In contrast, IASSLBs with a 1 or 2 nm LPO coating had an initial discharge capacity of 138 and 143 mAh g^{-1} at 3.6 V, respectively, and exhibited high capacity retention rate of 88% and 92.3% after 400 cycles, which indicates that coating nanofilms on the surface of ISE using the ALD method can effectively

passivate the interface of halide SSEs and break free from the traps of parasitic chemical reactions, achieving some positive characteristics of high-capacity halide ion conductors during cycling (Figure 14K).

4.2 | Strong interface binding

Han et al. prepared a Ca, Nb-doped garnet type ISE (LLCZN) and deposited a layer of Al_2O_3 on the Li metal side of the ISEs by ALD (Figure 15A).[18] The Al_2O_3 deposition layer upgrades the interfacial wettability, allowing Li metal to have more complete contact with ISEs, while reducing the obstruction of cracks and pores at the interface as shown in Figure 15A. Moreover, the presence of Al_2O_3 reduces the grain boundary/interface area specific resistances from 3500 to 150 $\Omega\,cm^2$ (Figure 15B). The interface impedance and Li-ion transport ability of the interface between garnet and Li metal were further evaluated in the d.c. Li electroplating/stripping experiments. Symmetrical cells containing ALD coating remained stable at $\sim$13 mV at a current density of 0.1 mA cm^{-2} (Figure 15B). In contrast, control cells without ALD coating exhibit noise potential with excessive voltage polarization due to uneven Li$^+$ transport over the interface. Through first-principles calculation, it is found that the interface binding energy between ISEs and Li metal without Al_2O_3 coating is calculated as 1.6 eV nm^{-2}, because the ISEs surface is covered with thin Li_2CO_3 layer owing to manufacturing in air (Figure 15C). On the contrary, the binding energy between ISEs with Al_2O_3 coating and Li metal is as high as 6.0–11.4 eV nm^{-2}, which reveals that strong interface bonding improves the wettability of Li metal on Al_2O_3-coated ISEs. Secondly, the chemical interface stability of garnet/Li metal was also calculated from first-principles calculation. The doped garnet LLCZN employed in this investigation shows phase stability to Li metal and phase equilibrium of additional decomposition components CaO and Nb, as evidenced by the Li grand potential phase map of the LLZO system in Figure 15C. The Li grand canonical phase diagram also shows that the lithiated alumina formed by the garnet LLZO via covering the Al_2O_3 coating can stabilize the −0.06 eV of equilibrium Li chemical potential to −1.23 eV, therefore the introduction of ALD-Al_2O_3 coating protects the garnet from decomposition by reacting with the metal Li. Wang et al. successfully formed a thin and compact nano ZnO coating on the surface of 3D porous garnet-based ISEs using ALD technology, and was reduced by molten Li to form LiZn alloy, which improved the wettability of the electrolyte/Li metal interface (Figure 15D).[19] The cross-sectional SEM results of garnet-based ISEs indicate that there is

continuous and firm contact between the lithium metal and garnet electrolyte as a result of the excellent reactivity and wettability of the ultra-thin ZnO coating with molten Li (Figure 15E). The ASR resistance value of Li/Garnet/Li symmetrical cells coated with $\sim$30 nm ZnO is about 90 $\Omega\,cm^2$, which is one-twentieth of that of unoptimized Li/Garnet/Li symmetrical cells. After 50 h of stripping/electroplating at galvanostatic cycling, the ASR resistance further decreased to 20 $\Omega\,cm^2$, which is attributed to further lithiation and activation of the interface layer during operation (Figure 15F).

4.3 | Reduce interfacial energy

Ren et al. confirmed in STEM/EDX that the 5 nm ALD-Al_2O_3 coating undergoes Al element diffusion into the bulk LCO after annealing, rather than through grain boundary diffusion, which brings instability to the cubic phase LLCZTO (Figure 16A).[20] In the analysis of the LCO/LLCZTO interface using the time-of-flight secondary ion mass spectrometry (ToF-SIMS) system, it was observed that the uneven interface of LLCZTO without coating resulted in cross-diffusion of Co, La, Zr, and Ca along with accumulation of Li, which represent the formation of tetragonal impurity phases in garnet (Figure 16B). This phenomenon can be further proven in XRD and TEM that after annealing at 800°C, no impurity phases such as tetragonal garnet were detected at the interface of cubic garnet/LCO with Al_2O_3 coating, which would appear in samples without coating (Figure 16C). Additionally, XRD also discovers the existence of (003) oriented LCO phases dominated by interfacial energy growth in the uncoated LCO/LLCZTO interface.[162] Compared with (101) and (104) orientations, grains with (003) orientation, especially those in direct contact with garnet electrolytes, are basically a blocking agent for facile lithiation/delithation of LCO.[163,164] After inserting the ALD-Al_2O_3 coating, the preferred orientation of the film (101) and (104) is restored, demonstrating that the main function of the Al_2O_3 coating is to reduce interfacial energy and prevent side reactions. This provides a strong explanation for the higher reversible capacity and decreasing total impedance exhibited by LCO/LLCZTO/Li batteries containing ALD-Al_2O_3 (Figure 16D). Rajendran et al. deposited h-BN with a thickness of approximately 3 nm on the surface of $Li_{6.5}La_3Zr_{1.5}Ta_{0.5}O_{12}$ (LLZT) using in situ ALD using tris (dimethylamino) borane and ammonia precursor at 450°C.[21] As shown in the FE-SEM image, there will be approximately 1–3 μm gap when Li metal comes into contact with the synthesized LLZT (Figure 16E). In
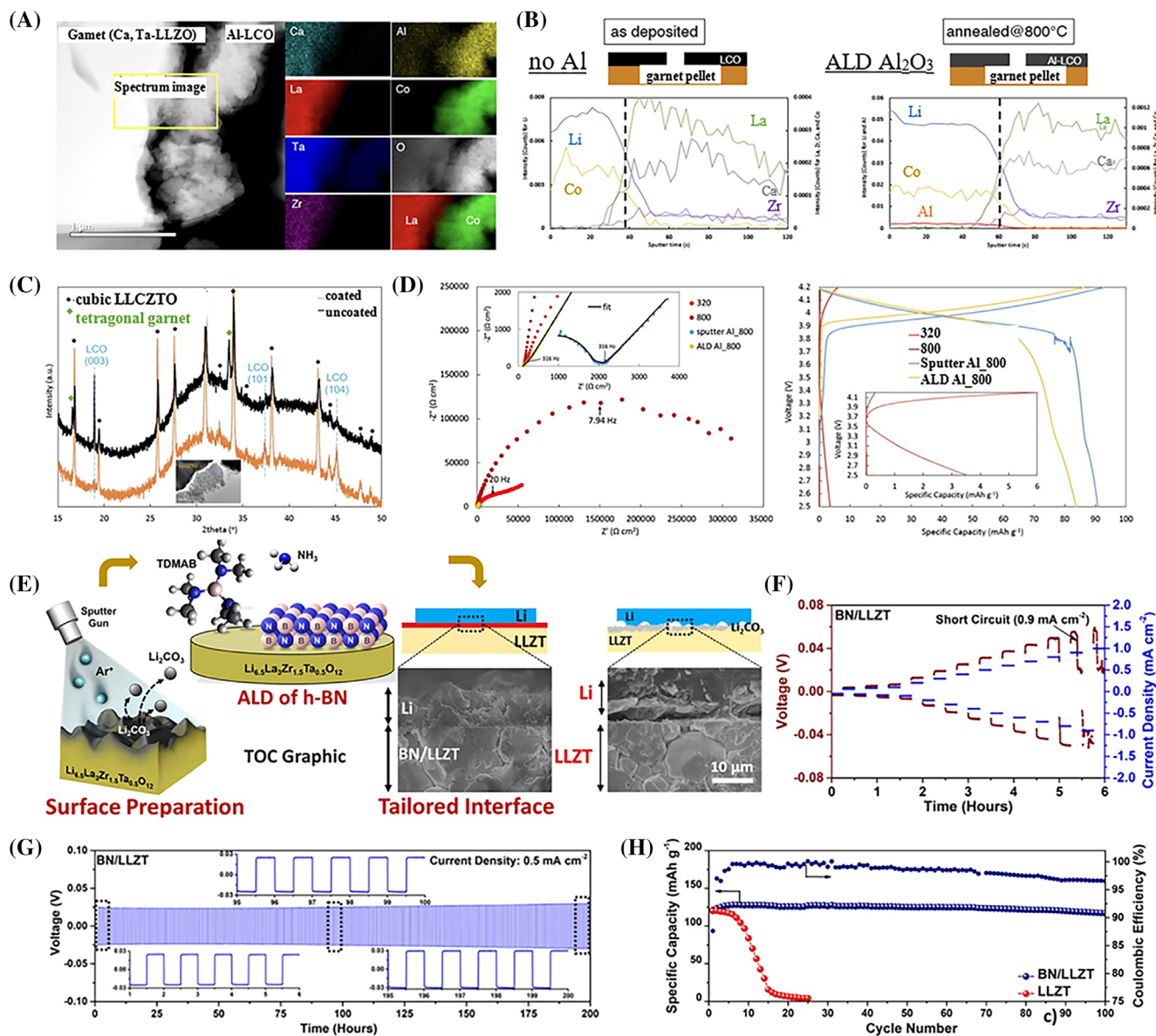
FIGURE 16 (A) Al_2O_3 coated LCO/LLCZTO interface with the chosen region mapped by STEM imaging and EDX elemental analysis at 800°C. (B) Before and after annealing at 800°C, ToF-SIMS depth profiles across the uncoated and ALD Al_2O_3 coated LCO/LLCZTO interfaces were obtained. (C) XRD patterns of 800°C annealed LCO/LLCZTO stacks with and without Al_2O_3 covering. An inset TEM diagram of the stack with an Al_2O_3 covering depicts the development of the majority of the LCO grains in the [110] direction. (D) Electrochemical performance of LCO/LLCZTO/Li cells annealed at 320 and 800°C with and without an Al_2O_3 covering. Reproduced with permission.[20] Copyright 2022, IOP Publishing. (E) Illustration diagram of LLZT surface cleaning via Ar^+ sputtering and surface wetting property of metallic Li with as-synthesized LLZT and h-BN-coated surface-cleaned LLZT. (F) Employing the BN/LLZT electrolyte for CCD measuring. (G, H) Electrochemical performances of the symmetrical cells and IASSLBs. Reproduced with permission.[21] Copyright 2021, American Chemical Society.

contrast, BN/LLZT exhibits extraordinary adhesion to metal Li. Notably, no voids or gaps were observed at the interface with the BN coating, indicating a strong bond between BN/LLZT and metallic Li. According to the reports, the advance in wettability may be a reflection of the weak Lewis acid–base interactions of h-BN.[165] Moreover, it was observed that the h-BN coating increased the critical current density (CCD) of

Li|LLZT|Li symmetric batteries in customized Swagelok cells at a pressure of 126 kPa (Figure 16F). Direct current (d.c.) Li electroplating/stripping experiments conducted at different current densities of 60°C showed that BN/LLZT symmetric cells maintained an ultra-low overpotential of 10–12 mV after running for 400 h, which confirms that BN/LLZT has improved interface ion transport and remains consistent with
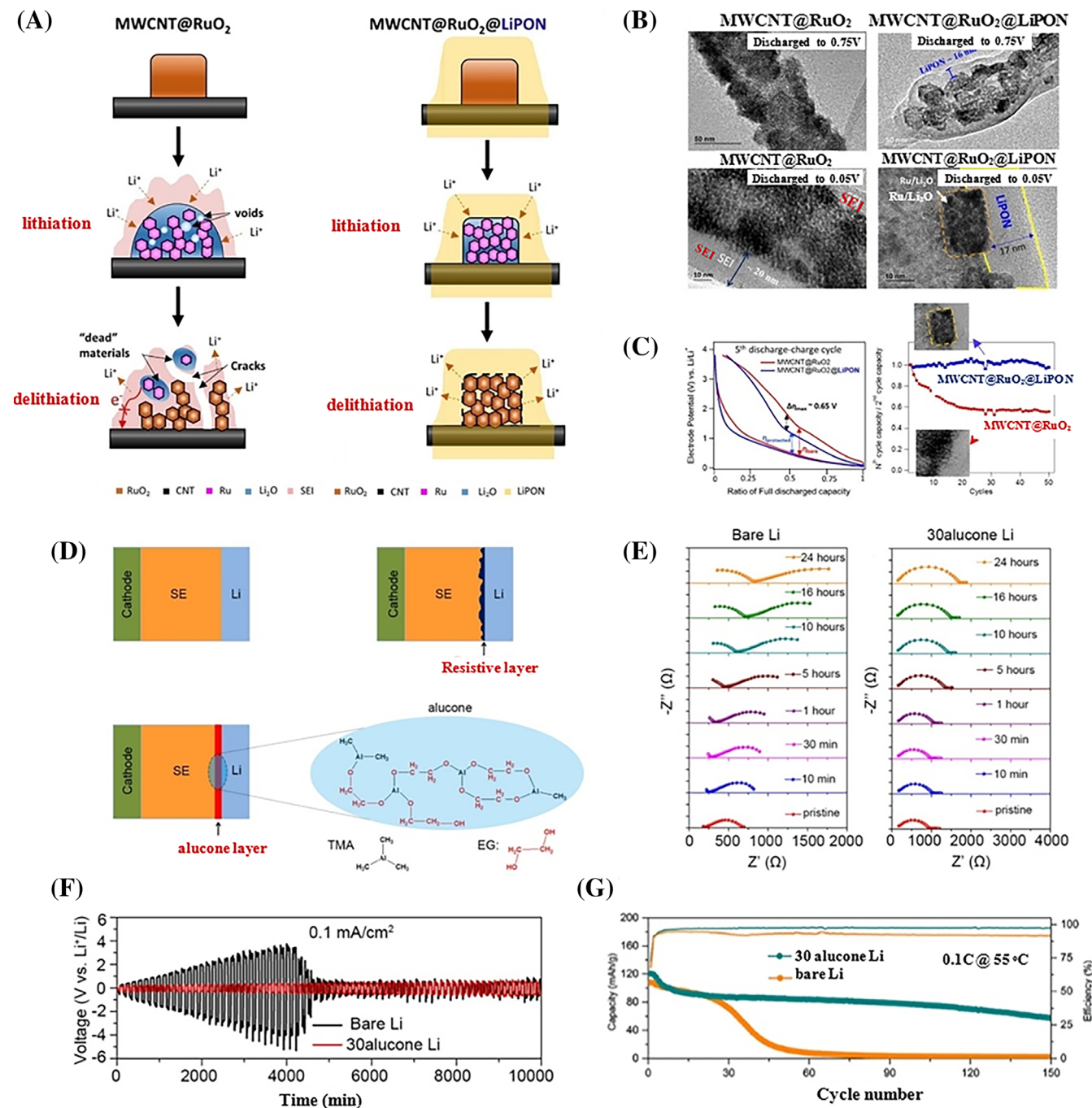
FIGURE 17 (A) Mechanism diagrams contrast the naked MWCNT@RuO$_2$ electrode with the LiPON-protected MWCNT@RuO$_2$. (B) TEM diagrams of 3D MWCNT@RuO$_2$/LiPON-protected MWCNT@RuO$_2$ electrodes discharged to 0.75/0.05 V. (C) Analysis of the discharge–charge profiles of bare RuO$_2$ versus LiPON-protected RuO$_2$ via overpotential and normalized capacities. Reproduced with permission.[23] Copyright 2016, American Chemical Society. (D) Schematic diagram of IASSLB based on ISEs. (E) Electrochemical resistance spectra of Li-Li symmetric cells. (F) Comparison of the Li plating/stripping behavior of Li symmetric cells at 0.1 mA cm^{-2} of current density and 0.1 mAh cm^{-2} of area. (G) Long-term cycling performance of LiCoO$_2$-based IASSLBs at 55°C. Reproduced with permission.[84] Copyright 2018, Elsevier.

previous results (Figure 16G). Furthermore, the electrochemical behavior differences between synthesized LLZT and those containing h-BN/LLZT were measured in IASSLBs. It would be capable of understanding from

Figure 16H that the synthesized LLZT rapidly decays after several cycles due to electrochemical and interfacial mechanical instability, while BN/LLZT exhibits a reversible capacity of 130 mAh g^{-1} over 100 cycles.

4.4 | Others

According to the report, Lin et al. revealed the mechanical constraint mechanism of LiPON coating in double-coated multiwalled carbon nanotubes (MWCNT@RuO$_2$@LiPON) with ALD, which is to maintain the dense structure arrangement of Ru and Li$_2$O discharge products to ameliorate the electronic connectivity of electrode materials along with the Li$^+$ transport path between ISEs and electrode material (Figure 17A).[23] TEM represents that when the MWCNT@RuO$_2$ electrode discharge (lithiation) reaches 0.75 V–0.05 V, the tetragonal crystal of RuO$_2$ is crushed into small nanoparticles, while the electrolyte further decomposes to form 20 nm SEI (Figure 17B). In contrast, the MWCNT@RuO$_2$@LiPON electrode maintains its structure and the conformal LiPON layer remains intact. Another noteworthy observation is that the tetragonal shape of RuO$_2$ deposition on the MWCNT@RuO$_2$ electrode is completely destroyed into small Ru nanoparticles after lithiation. The sharp twists (yellow dashed lines) in the square shape of the MWCNT@RuO$_2$@LiPON electrode during deposition still reserve, which strongly indicates that the ion conductive LiPON layer provides mechanical constraints to maintain the structural integrity of the RuO$_2$ electrode throughout the lithiation process. The side reactions that occur during the charging process form insulating lithium compounds, namely Li$_2$O, which make for an increase in overpotential during the charging process. As shown in Figure 17C, the LiPON coating effectively reduces this overpotential when the electrode cycles for five cycles, MWCNT@RuO$_2$@LiPON has reduced by 0.65 V compared to unprotected overpotential. As expected, without LiPON protection MWCNT@RuO$_2$ electrode (red) loses capacity with cycling and only retains 55% of the second discharge capacity after 20 cycles. In stark contrast to this MWCNT@RuO$_2$@LiPON (blue in Figure 17C) retained >95% of the second cycle capacity in 50 cycles. Sun's group applied an inorganic organic hybrid intermediate layer (alucone) between Li metal and sulfide solid electrolyte (Li$_{10}$SnP$_2$S$_{12}$, LSPS) through MLD interface engineering.[84] This inorganic organic hybrid intermediate layer has more favorable mechanical properties than pure inorganic coatings (such as Al$_2$O$_3$), which is conducive to regulating the stress/strain caused by changes in electrode volume (Figure 17D). Moreover, the Nyquist diagram of Li symmetric cells with Li/LPS/Li structure coated with alucone exhibits a more stable interface resistance. On the contrary, the interface between unprotected Li and LSPS is a mixed ion-electron conductor due to side reactions, and this material obviously cannot block the electron transfer at the anode interface, which triggers an increasing interface impedance as the side reactions continue to occur (Figure 17E). The results of long-term cycling measurements on both symmetrical and full batteries were consistent with the Nyquist plot data, indicating clearly that Li metal with MLD coating can be successfully applied to IASSLBs without affecting the energy density of IASSLB (Figure 17F,G).

5 | CONCLUSIONS AND PERSPECTIVES

This review overviews the main attractiveness of IASSLBs as one of the most promising systems for next-generation batteries and the significant challenges they face, with a focus on the development and understanding of ALD/MLD technology in the application of ISE interface modification. Compared to other common coating methods, ALD/MLD can fine-tune the composition and thickness of the coating on the electrode at the atomic/molecular level to achieve electrode interfaces with multiple functions: (i) passivation, (ii) strong interface binding, (iii) reduce interfacial energy, and so on. Ultimately, ALD/MLD improved coated electrodes exhibit enhanced electrochemical mechanical compatibility with various ISEs on the cathode or anode side, especially for sensitive sulfide-based electrolytes.

The future perspectives of ALD/MLD technologies for interface engineering in SSLBs and even all-solid-state batteries (ASSBs) are exciting and hold great promise for enhancing battery performance and longevity. Following are some key challenges and potential developments:

1. Implementing ALD/MLD technologies on a grand scale for interface engineering in SSLBs and the manufacturing of ASSBs is feasible, but it comes with several challenges and considerations. Specifically, (i) while ALD/MLD technologies are well-established in research and smaller-scale production, scaling these processes for mass manufacturing can be complex. Equipment costs, throughput rates, and cycle times must be addressed; (ii) the materials used in ALD/MLD must be compatible with the battery components and processes. Finding suitable precursors that can work effectively at the required scale is essential; (iii) the initial investment for ALD/MLD systems can be high, and ongoing operational costs must be justified by the performance improvements in the batteries; (iv) integrating ALD/MLD with existing manufacturing processes for interface engineering in SSLBs and ASSBs requires careful planning to ensure compatibility and efficiency. While there are significant challenges to overcome, the potential benefits of ALD and MLD technologies make them promising candidates for large-scale implementation in interface

engineering in SSLBs and ASSBs manufacturing. Ongoing research and development will likely focus on optimizing these processes, reducing costs, and enhancing scalability to realize their full potential in commercial applications.

2. Further research is necessary on the function and working mechanism of ALD/MLD thin films at the IASSLBs interface. Advanced and diverse spectral/imaging characterization techniques, including in situ NDP, XAS/X-CT, ACTEM/STEM-HAADF, and so on, with high-resolution technology. Particularly, the in situ analysis is a vital tool that can deeply understand the dynamic evolution process of interfaces, interface stress distribution status, and volume changes of the full battery during battery cycling. Characterization combined with ALD/MLD is an ideal guidance for researchers in selecting explicit methods for remarkable interfaces.

3. For Li/ISE interfaces, many methods can reduce the interface resistance to a level close to that of liquid batteries. Nevertheless, MLD technology has limited research on Li-ion diffusion at electrode/ISEs interface, formation of interface facial mask, and interface reaction. Further exploration and theoretical calculations should be conducted to guide for construction of stable IASSLB systems.

4. Past research was mainly focused on the improvement of interface contact, the chemical stability between electrodes and electrolytes, and the elimination of the space charge layer. It provokes the lack of in-depth research on the real voltage window of ISEs, so that electrolytes generally operate in the range higher than their respective voltage windows, causing a series of interface side reactions. In particular, the reaction products are mostly ion-poor conductors after matching with the high-voltage positive electrode, which hinders the transmission of Li ions.

5. To promote interface behavior, ALD/MLD must tackle the challenges posed by the strong oxidation of high-voltage positive electrodes and the reduction of Li negative electrodes from both dynamic (interface passivation) and thermodynamic perspectives. This involves the construction of a stable multi-component phase space. One approach is to utilize artificial intelligence (AI) and machine learning models to identify and rank possible chemical systems. These findings can then be combined with thermodynamic calculations to assess the energy difference between the studied phases and the thermodynamically stable phases across various environments. This strategy offers valuable insights for the development and improvement of new materials in ALD/MLD.[166,167]

In summary, the application of ALD/MLD technologies in interface engineering SSLBs presents significant opportunities for advancements in battery performance, safety, and sustainability. As research continues and challenges related to scalability and cost are addressed, these technologies could play a pivotal role in the commercialization of SSLBs, making them a cornerstone of future energy storage solutions.

CONFLICT OF INTEREST STATEMENT

The authors declare no conflicts of interest.

ORCID

Gaixia Zhang https://orcid.org/0000-0002-5340-8961
Shuhui Sun https://orcid.org/0000-0002-0508-2944

REFERENCES

1. Winter M, Brodd RJ. What are batteries, fuel cells, and supercapacitors? *Chem Rev*. 2004;104(10):4245-4269.
2. Bruce PG, Scrosati B, Tarascon JM. Nanomaterials for rechargeable lithium batteries. *Angew Chem Int Ed Engl*. 2008;47(16):2930-2946.
3. Goodenough JB. Evolution of strategies for modern rechargeable batteries. *Accounts Chem Res*. 2013;46(5):1053-1061.
4. Goodenough JB, Park KS. The Li-ion rechargeable battery: a perspective. *J Am Chem Soc*. 2013;135(4):1167-1176.
5. Bruce PG, Freunberger SA, Hardwick LJ, Tarascon JM. Li-O$_2$ and Li-S batteries with high energy storage. *Nat Mater*. 2012;11(1):19-29.
6. Ma BC, Li RH, Zhu HT, et al. Stable oxyhalide-nitride fast ionic conductors for all-solid-state Li metal batteries. *Adv Mater*. 2024;36(30):2402324.
7. Manthiram A, Yu X, Wang S. Lithium battery chemistries enabled by solid-state electrolytes. *Nat Rev Mater*. 2017;2(4):16103.
8. Yoshiyuki I, Chen L, Mitsuru I, et al. High ionic conductivity in lithium lanthanum titanate. *Solid State Commun*. 1993;86(10):689-693.
9. Famprikis T, Canepa P, Dawson JA, Islam MS, Masquelier C. Fundamentals of inorganic solid-state electrolytes for batteries. *Nat Mater*. 2019;18(12):1278-1291.
10. Yin YC, Yang JT, Luo JD, et al. A LaCl-based lithium superionic conductor compatible with lithium metal. *Nature*. 2023;616(7955):77-83.
11. Song LB, Li RH, Zhu HT, et al. Deeply lithiated carbonaceous materials for great lithium metal protection in all-solid-state batteries. *Adv Mater*. 2024;36(26):2400165.

12. Zhang S, Ma J, Dong SM, Cui GL. Designing all-solid-state batteries by theoretical computation: a review. *Electrochem Energy Rev.* 2023;6(1):4.

13. Liu QR, Chen QQ, Tang YB, Cheng HM. Interfacial modification, electrode/solid-electrolyte engineering, and monolithic construction of solid-state batteries. *Electrochem Energy Rev.* 2023;6(1):15.

14. Sung J, Kim SY, Harutyunyan A, et al. Ultra-thin lithium silicide interlayer for solid-state lithium-metal batteries. *Adv Mater.* 2023;35(22):2210835.

15. Jin E, Su J, Hou H, et al. Electro-chemo-mechanically stable and sodiophilic interface for Na metal anode in liquid-based and solid-state batteries. *Adv Mater.* 2024;36(35):e2406837.

16. Guo HJ, Sun YP, Zhao Y, et al. Surface degradation of single-crystalline Ni-rich cathode and regulation mechanism by atomic layer deposition in solid-state lithium batteries. *Angew Chem Int Ed Engl.* 2022;61(48):e202211626.

17. Liu J, Lu DP, Zheng JM, et al. Minimizing polysulfide shuttle effect in lithium-ion sulfur batteries by anode surface passivation. *ACS Appl Mater Inter.* 2018;10(26):21965-21972.

18. Han XG, Gong YH, Fu K, et al. Negating interfacial impedance in garnet-based solid-state Li metal batteries. *Nat Mater.* 2017;16(5):572-579.

19. Wang CW, Gong YH, Liu BY, et al. Conformal, nanoscale ZnO surface modification of garnet-based solid-state electrolyte for lithium metal anodes. *Nano Lett.* 2017;17(1):565-571.

20. Ren YY, Wachsman ED. All solid-state Li/LLZO/LCO battery enabled by alumina interfacial coating. *J Electrochem Soc.* 2022;169(4):040529.

21. Rajendran S, Pilli A, Omolere O, Kelber J, Arava LMR. An all-solid-state battery with a tailored electrode-electrolyte interface using surface chemistry and interlayer-based approaches. *Chem Mater.* 2021;33(9):3401-3412.

22. Deng T, Ji X, Zhao Y, et al. Tuning the anode-electrolyte interface chemistry for garnet-based solid-state Li metal batteries. *Adv Mater.* 2020;32(23):2000030.

23. Lin CF, Noked M, Kozen AC, et al. Solid electrolyte lithium phosphous oxynitride as a protective nanocladding layer for 3D high-capacity conversion electrodes. *ACS Nano.* 2016;10(2):2693-2701.

24. He L, Chen C, Kotobuki M, Zheng F, Zhou H, Lu L. A new approach for synthesizing bulk-type all-solid-state lithium-ion batteries. *J Mater Chem A.* 2019;7(16):9748-9760.

25. Wang X, Yushin G. Chemical vapor deposition and atomic layer deposition for advanced lithium ion batteries and supercapacitors. *Energ Environ Sci.* 2015;8(7):1889-1904.

26. Huang X, Lu Y, Jin J, et al. Method using water-based solvent to prepare $Li_7La_3Zr_2O_{12}$ solid electrolytes. *ACS Appl Mater Interfaces.* 2018;10(20):17147-17155.

27. Ahn C-W, Choi J-J, Ryu J, et al. Microstructure and ionic conductivity in $Li_7La_3Zr_2O_{12}$ film prepared by aerosol deposition method. *J Electrochem Soc.* 2014;162(1):A60-A63.

28. Sakuda A, Hayashi A, Tatsumisago M. Sulfide solid electrolyte with favorable mechanical property for all-solid-state lithium battery. *Sci Rep.* 2013;3(1):2261.

29. Lobe S, Bauer A, Uhlenbruck S, Fattakhova-Rohlfing D. Physical vapor deposition in solid-state battery development: from materials to devices. *Adv Sci (Weinh).* 2021;8(11):e2002044.

30. Hayashi T, Okada J, Toda E, et al. Electrochemical effect of lithium tungsten oxide modification on $LiCoO_2$ thin film electrode. *J Power Sources.* 2015;285:559-567.

31. Lobe S, Dellen C, Finsterbusch M, et al. Radio frequency magnetron sputtering of $Li_7La_3Zr_2O_{12}$ thin films for solid-state batteries. *J Power Sources.* 2016;307:684-689.

32. Minami K, Mizuno F, Hayashi A, Tatsumisago M. Lithium ion conductivity of the $Li_2S–P_2S_5$ glass-based electrolytes prepared by the melt quenching method. *Solid State Ion.* 2007;178(11–12):837-841.

33. Puurunen RL. Surface chemistry of atomic layer deposition: a case study for the trimethylaluminum/water process. *J Appl Phys.* 2005;97(12):121301.

34. Steven GM. Atomic layer deposition: an overview. *Chem Rev.* 2010;110(1):111-131.

35. Pirayesh P, Tantratian K, Amirmaleki M, et al. From nanoalloy to nano-laminated interfaces for highly stable alkali-metal anodes. *Adv Mater.* 2023;35(29):e2301414.

36. Mallick BC, Hsieh C-T, Yin K-M, Gandomi YA, Huang K-T. Review—on atomic layer deposition: current progress and future challenges. *ECS J Solid State Sci Technol.* 2019;8(4):N55-N78.

37. Mallick BC, Hsieh CT, Yin KM, Li J, Ashraf Gandomi Y. Linear control of the oxidation level on graphene oxide sheets using the cyclic atomic layer reduction technique. *Nanoscale.* 2019;11(16):7833-7838.

38. Gu S, Hsieh C-T, Mallick BC, et al. Amino-functionalization on graphene oxide sheets using an atomic layer amidation technique. *J Mater Chem C.* 2020;8(2):700-705.

39. Zheng JM, Wu XB, Yang Y. A comparison of preparation method on the electrochemical performance of cathode material $Li[Li_{0.2}Mn_{0.54}Ni_{0.13}Co_{0.13}]O_2$ for lithium ion battery. *Electrochim Acta.* 2011;56(8):3071-3078.

40. Meng X, Yang XQ, Sun X. Emerging applications of atomic layer deposition for lithium-ion battery studies. *Adv Mater.* 2012;24(27):3589-3615.

41. Puurunen RL. A short history of atomic layer deposition: Tuomo Suntola's atomic layer epitaxy. *Chem Vapor Depos.* 2014;20(10–12):332-344.

42. Nishizawa J, Abe H, Kurabayashi T. Molecular layer epitaxy. *J Electrochem Soc.* 1985;132(5):1197-1200.

43. Choi H, Shin S, Jeon H, et al. Fast spatial atomic layer deposition of Al_2O_3 at low temperature (<100°C) as a gas permeation barrier for flexible organic light-emitting diode displays. *J Vac Sci Technol A.* 2016;34(1):01A121.

44. Weimer AW. Particle atomic layer deposition. *J Nanopart Res.* 2019;21(1):9.

45. Cai JY, Ma ZY, Wejinya U, et al. A revisit to atomic layer deposition of zinc oxide using diethylzinc and water as precursors. *J Mater Sci.* 2019;54(7):5236-5248.

46. Heo J, Hock AS, Gordon RG. Low temperature atomic layer deposition of tin oxide. *Chem Mater.* 2010;22(17):4964-4973.

47. Groner MD, Fabreguette FH, Elam JW, George SM. Low-temperature Al_2O_3 atomic layer deposition. *Chem Mater.* 2004;16(4):639-645.

48. Hamalainen J, Ritala M, Leskela M. Atomic layer deposition of noble metals and their oxides. *Chem Mater.* 2014;26(1):786-801.

49. Mackus AJM, Schneider JR, MacIsaac C, Baker JG, Bent SF. Synthesis of doped, ternary, and quaternary materials by atomic layer deposition: a review. *Chem Mater*. 2018;31(4):1142-1183.

50. Zhao W, Duan Y. Advanced applications of atomic layer deposition in perovskite-based solar cells. *Adv Photonics Res*. 2021;2(7):2100011.

51. Sun Q, Lau KC, Geng D, Meng X. Atomic and molecular layer deposition for superior lithium-sulfur batteries: strategies, performance, and mechanisms. *Batteries & Supercaps*. 2018;1(2):41-68.

52. Yu F, Du L, Zhang G, Su F, Wang W, Sun S. Electrode engineering by atomic layer deposition for sodium-ion batteries: from traditional to advanced batteries. *Adv Funct Mater*. 2019;30(9):1906890.

53. Zhao Z, Huang G, Kong Y, et al. Atomic layer deposition for electrochemical energy: from design to industrialization. *Electrochem Energy Rev*. 2022;5(S1):31.

54. Li Z, Su J, Wang X. Atomic layer deposition in the development of supercapacitor and lithium-ion battery devices. *Carbon*. 2021;179:299-326.

55. Yoshimura T, Tatsuura S, Sotoyama W. Polymer-films formed with monolayer growth steps by molecular layer deposition. *Appl Phys Lett*. 1991;59(4):482-484.

56. Yoshimura T, Tatsuura S, Sotoyama W, Matsuura A, Hayano T. Quantum wire and dot formation by chemical vapor-deposition and molecular layer deposition of one-dimensional conjugated polymer. *Appl Phys Lett*. 1992;60(3):268-270.

57. Du Y, George SM. Molecular layer deposition of nylon 66 films examined using in situ FTIR spectroscopy. *J Phys Chem C*. 2007;111(24):8509-8517.

58. Adarnczyk NM, Dameron AA, George SM. Molecular layer deposition of poly(p-phenylene terephthalamide) films using terephthaloyl chloride and p-phenylenediamine. *Langmuir*. 2008;24(5):2081-2089.

59. Loscutoff PW, Lee HBR, Bent SF. Deposition of ultrathin polythiourea films by molecular layer deposition. *Chem Mater*. 2010;22(19):5563-5569.

60. Ivanova TV, Maydannik PS, Cameron DC. Molecular layer deposition of polyethylene terephthalate thin films. *J Vac Sci Technol A*. 2012;30(1):01A121.

61. Zhou H, Bent SF. Highly stable ultrathin carbosiloxane films by molecular layer deposition. *J Phys Chem C*. 2013;117(39):19967-19973.

62. Giedraityte Z, Sundberg P, Karppinen M. Flexible inorganic–organic thin film phosphors by ALD/MLD. *J Mater Chem C*. 2015;3(47):12316-12321.

63. Nisula M, Karppinen M. In situ lithiated quinone cathode for ALD/MLD-fabricated high-power thin-film battery. *J Mater Chem A*. 2018;6(16):7027-7033.

64. Sarkar D, Ishchuk S, Taffa DH, et al. Oxygen-deficient Titania with adjustable band positions and defects; molecular layer deposition of hybrid organic–inorganic thin films as precursors for enhanced Photocatalysis. *J Phys Chem C*. 2016;120(7):3853-3862.

65. Su Y, Hao JL, Liu XS, Yang Y. Progress of atomic layer deposition and molecular layer deposition in the development of all-solid-state lithium batteries. *Batteries & Supercaps*. 2022;6(1):e202200359.

66. Zhao Y, Zhang L, Liu J, et al. Atomic/molecular layer deposition for energy storage and conversion. *Chem Soc Rev*. 2021;50(6):3889-3956.

67. Woo JH, Trevey JE, Cavanagh AS, et al. Nanoscale interface modification of $LiCoO_2$ by Al_2O_3 atomic layer deposition for solid-state Li batteries. *J Electrochem Soc*. 2012;159(7):A1120-A1124.

68. Liu YL, Sun Q, Zhao Y, et al. Stabilizing the Interface of NASICON solid electrolyte against Li metal with atomic layer deposition. *ACS Appl Mater Inter*. 2018;10(37):31240-31248.

69. Davis AL, Garcia-Mendez R, Wood KN, et al. Electro-chemo-mechanical evolution of sulfide solid electrolyte/Li metal interfaces: operando analysis and ALD interlayer effects. *J Mater Chem A*. 2020;8(13):6291-6302.

70. Fan ZJ, Ding B, Zhang TF, et al. Solid/solid interfacial architecturing of solid polymer electrolyte-based all-solid-state lithium-sulfur batteries by atomic layer deposition. *Small*. 2019;15(46):1903952.

71. Cortes FJQ, Lewis JA, Tippens J, Marchese TS, McDowell MT. How metallic protection layers extend the lifetime of NASICON-based solid-state lithium batteries. *J Electrochem Soc*. 2019;167(5):050502.

72. Li X, Ren ZH, Banis MN, et al. Unravelling the chemistry and microstructure evolution of a cathodic interface in sulfide-based all-solid-state Li-ion batteries. *ACS Energy Lett*. 2019;4(10):2480-2488.

73. Liu XS, Shi JW, Zheng BZ, et al. Constructing a high-energy and durable single-crystal NCM811 cathode for all-solid-state batteries by a surface engineering strategy. *ACS Appl Mater Inter*. 2021;13(35):41669-41679.

74. Wang CH, Li X, Zhao Y, et al. Manipulating interfacial nano-structure to achieve high-performance all-solid-state lithium-ion batteries. *Small Methods*. 2019;3(10):1900261.

75. Vinado C, Wang SY, He Y, et al. Electrochemical and interfacial behavior of all solid state batteries using $Li_{10}SnP_2S_{12}$ solid electrolyte. *J Power Sources*. 2018;396:824-830.

76. Liang JN, Hwang S, Li S, et al. Stabilizing and understanding the interface between nickel-rich cathode and PEO-based electrolyte by lithium niobium oxide coating for high-performance all-solid-state batteries. *Nano Energy*. 2020;78:105107.

77. Deng SX, Li X, Ren ZH, et al. Dual-functional interfaces for highly stable Ni-rich layered cathodes in sulfide all-solid-state batteries. *Energy Storage Mater*. 2020;27:117-123.

78. Zhao FP, Zhao Y, Wang J, et al. Tuning bifunctional interface for advanced sulfide-based all-solid-state batteries. *Energy Storage Mater*. 2020;33:139-146.

79. Kazyak E, Chen KH, Chen YX, Cho TH, Dasgupta NP. Enabling 4C fast charging of lithium-ion batteries by coating graphite with a solid-state electrolyte. *Adv Energy Mater*. 2022;12(1):2102618.

80. Kitsche D, Tang YS, Hemmelmann H, et al. Atomic layer deposition derived zirconia coatings on Ni-rich cathodes in solid-state batteries: correlation between surface constitution and cycling performance. *Small Sci*. 2023;3(2):2200073.

81. Jin Y, Yu H, He XQ, Liang XH. Stabilizing the Interface of all-solid-state electrolytes against cathode electrodes by atomic layer deposition. *ACS Appl Energ Mater*. 2022;5(1):760-769.

82. Kitsche D, Tang YS, Ma Y, et al. High performance all-solid-state batteries with a Ni-rich NCM cathode coated by atomic layer deposition and lithium thiophosphate solid electrolyte. *ACS Appl Energ Mater.* 2021;4(7):7338-7345.

83. Deng SX, Sun YP, Li X, et al. Eliminating the detrimental effects of conductive agents in sulfide-based solid-state batteries. *ACS Energy Lett.* 2020;5(4):1243-1251.

84. Wang CH, Zhao Y, Sun Q, et al. Stabilizing interface between $Li_{10}SnP_2S_{12}$ and Li metal by molecular layer deposition. *Nano Energy.* 2018;53:168-174.

85. Zhang SM, Zhao Y, Zhao FP, et al. Gradiently sodiated alucone as an interfacial stabilizing strategy for solid-state Na metal batteries. *Adv Funct Mater.* 2020;30(22):2001118.

86. Kazyak E, Shin M, LePage WS, Cho TH, Dasgupta NP. Molecular layer deposition of Li-ion conducting "Lithicone" solid electrolytes. *Chem Commun.* 2020;56(99):15537-15540.

87. Nisula M, Karppinen M. Atomic/molecular layer deposition of lithium terephthalate thin films as high rate capability Li-ion battery anodes. *Nano Lett.* 2016;16(2):1276-1281.

88. Kamaya N, Homma K, Yamakawa Y, et al. A lithium superionic conductor. *Nat Mater.* 2011;10(9):682-686.

89. Zhao Q, Liu XT, Stalin S, Khan K, Archer LA. Solid-state polymer electrolytes with in-built fast interfacial transport for secondary lithium batteries. *Nat Energy.* 2019;4(5):365-373.

90. Li S, Yang SJ, Liu GX, et al. A dynamically stable mixed conducting interphase for all-solid-state lithium metal batteries. *Adv Mater.* 2024;36(3):2307768.

91. Jia LA, Zhu JH, Zhang X, Guo BJ, Du YB, Zhuang XD. Li-solid electrolyte interfaces/interphases in all-solid-state Li batteries. *Electrochem Energy Rev.* 2024;7(1):12.

92. Monroe C, Newman J. The impact of elastic deformation on deposition kinetics at lithium/polymer interfaces. *J Electrochem Soc.* 2005;152(2):A396-A404.

93. Han FD, Westover AS, Yue J, et al. High electronic conductivity as the origin of lithium dendrite formation within solid electrolytes. *Nat Energy.* 2019;4(3):187-196.

94. Hou GM, Ma XX, Sun QD, et al. Lithium dendrite suppression and enhanced interfacial compatibility enabled by an ex situ SEI on Li anode for LAGP-based all-solid-state batteries. *ACS Appl Mater Inter.* 2018;10(22):18610-18618.

95. Yue J, Zhu XY, Han FD, et al. Long cycle life all-solid-state sodium ion battery. *ACS Appl Mater Inter.* 2018;10(46):39645-39650.

96. Wu BB, Wang SY, Lochala J, et al. The role of the solid electrolyte interphase layer in preventing Li dendrite growth in solid-state batteries. *Energ Environ Sci.* 2018;11(7):1803-1810.

97. Kasemchainan J, Zekoll S, Jolly DS, et al. Critical stripping current leads to dendrite formation on plating in lithium anode solid electrolyte cells. *Nat Mater.* 2019;18(10):1105-1111.

98. Porz L, Swamy T, Sheldon BW, et al. Mechanism of lithium metal penetration through inorganic solid electrolytes. *Adv Energy Mater.* 2017;7(20):1701003.

99. Doux JM, Nguyen H, Tan DHS, et al. Stack pressure considerations for room-temperature all-solid-state lithium metal batteries. *Adv Energy Mater.* 2020;10(1):1903253.

100. Sun F, Zielke L, Markotter H, et al. Morphological evolution of electrochemically plated/stripped lithium microstructures investigated by synchrotron x-ray phase contrast tomography. *ACS Nano.* 2016;10(8):7990-7997.

101. Crowther O, West AC. Effect of electrolyte composition on lithium dendrite growth. *J Electrochem Soc.* 2008;155(11):A806.

102. Cheng EJ, Sharafi A, Sakamoto J. Intergranular Li metal propagation through polycrystalline $Li_{6.25}Al_{0.25}La_3Zr_2O_{12}$ ceramic electrolyte. *Electrochim Acta.* 2017;223:85-91.

103. Swamy T, Park R, Sheldon BW, et al. Lithium metal penetration induced by electrodeposition through solid electrolytes: example in single-crystal $Li_6La_3ZrTaO_{12}$ garnet. *J Electrochem Soc.* 2018;165(16):A3648-A3655.

104. Peryez SA, Cambaz MA, Thangadurai V, Fichtnert M. Interface in solid-state lithium battery: challenges, progress, and outlook. *ACS Appl Mater Inter.* 2019;11(25):22029-22050.

105. Bulbula ST, Lu Y, Dong Y, Yang X-Y. Hierarchically porous graphene for batteries and supercapacitors. *New J Chem.* 2018;42(8):5634-5655.

106. Wenzel S, Leichtweiss T, Krüger D, Sann J, Janek J. Interphase formation on lithium solid electrolytes—an in situ approach to study interfacial reactions by photoelectron spectroscopy. *Solid State Ion.* 2015;278:98-105.

107. Murugan R, Thangadurai V, Weppner W. Fast lithium ion conduction in garnet-type $Li_7La_3Zr_2O_{12}$. *Angew Chem Int Ed Engl.* 2007;46(41):7778-7781.

108. Shin BR, Nam YJ, Oh DY, Kim DH, Kim JW, Jung YS. Comparative study of TiS_2/Li-in all-solid-state lithium batteries using glass-ceramic Li_3PS_4 and $Li_{10}GeP_2S_{12}$ solid electrolytes. *Electrochim Acta.* 2014;146:395-402.

109. Braga MH, Ferreira JA, Stockhausen V, Oliveira JE, El-Azab A. Novel Li_3ClO based glasses with superionic properties for lithium batteries. *J Mater Chem A.* 2014;2(15):5470-5480.

110. Lu X, Wu G, Howard JW, et al. Li-rich anti-perovskite Li_3OCl films with enhanced ionic conductivity. *Chem Commun (Camb).* 2014;50(78):11520-11522.

111. Tippens J, Miers JC, Afshar A, et al. Visualizing chemomechanical degradation of a solid-state battery electrolyte. *ACS Energy Lett.* 2019;4(6):1475-1483.

112. Aono H, Sugimoto E, Sadaoka Y, Imanaka N, Adachi G. Ionic conductivity of solid electrolytes based on lithium titanium phosphate. *J Electrochem Soc.* 1990;137(4):1023-1027.

113. Xu X, Wen Z, Wu X, Yang X, Gu Z. Lithium ion-conducting glass-ceramics of $Li_{1.5}Al_{0.5}Ge_{1.5}(PO_4)_3$-$xLi_2O$ (x = 0.0-0.20) with good electrical and electrochemical properties. *J Am Ceram Soc.* 2007;90(9):2802-2806.

114. Wenzel S, Weber DA, Leichtweiss T, Busche MR, Sann J, Janek J. Interphase formation and degradation of charge transfer kinetics between a lithium metal anode and highly crystalline $Li_7P_3S_{11}$ solid electrolyte. *Solid State Ion.* 2016;286:24-33.

115. Lepley ND, Holzwarth NAW, Du YA. Structures, Li+mobilities, and interfacial properties of solid electrolytes Li_3PS_4 and Li_3PO_4 from first principles. *Phys Rev B.* 2013;88(10):104103.

116. Chen B, Ju J, Ma J, et al. An insight into intrinsic interfacial properties between Li metals and $Li_{10}GeP_2S_{12}$ solid electrolytes. *Phys Chem Chem Phys.* 2017;19(46):31436-31442.

117. Shen YB, Zhang YT, Han SJ, Wang JW, Peng ZQ, Chen LW. Unlocking the energy capabilities of lithium metal electrode with solid-state electrolytes. *Joule.* 2018;2(9):1674-1689.

118. de Klerk NJJ, Wagemaker M. Space-charge layers in all-solid-state batteries; important or negligible? *ACS Appl Energy Mater*. 2018;1(10):5609-5618.

119. Haruta M, Shiraki S, Suzuki T, et al. Negligible "negative space-charge layer effects" at oxide-electrolyte/electrode interfaces of thin-film batteries. *Nano Lett*. 2015;15(3):1498-1502.

120. Yada C, Ohmori A, Ide K, et al. Dielectric modification of 5V-class cathodes for high-voltage all-solid-state lithium batteries. *Adv Energy Mater*. 2014;4(9):1301416.

121. Koerver R, Walther F, Aygun I, et al. Redox-active cathode interphases in solid-state batteries. *J Mater Chem A*. 2017; 5(43):22750-22760.

122. Banerjee A, Tang HM, Wang XF, et al. Revealing nanoscale solid-solid interfacial phenomena for long-life and high-energy all-solid-state batteries. *ACS Appl Mater Inter*. 2019; 11(46):43138-43145.

123. Zhang WB, Leichtweiss T, Culver SP, et al. The detrimental effects of carbon additives in $Li_{10}GeP_2S_{12}$-based solid-state batteries. *ACS Appl Mater Inter*. 2017;9(41):35888-35896.

124. Auvergniot J, Cassel A, Ledeuil JB, Viallet V, Seznec V, Dedryvere R. Interface stability of Argyrodite Li_6PS_5Cl toward $LiCoO_2$, $LiNi_{1/3}Co_{1/3}Mn_{1/3}O_2$, and $LiMn_2O_4$ in bulk all-solid-state batteries. *Chem Mater*. 2017;29(9):3883-3890.

125. Park K, Yu BC, Jung JW, et al. Electrochemical nature of the cathode interface for a solid-state lithium-ion battery: Interface between $LiCoO_2$ and garnet-$Li_7La_3Zr_2O_{12}$. *Chem Mater*. 2016;28(21):8051-8059.

126. Vardar G, Bowman WJ, Lu QY, et al. Structure, chemistry, and charge transfer resistance of the Interface between $Li_7La_3Zr_2O_{12}$ electrolyte and $LiCoO_2$ cathode. *Chem Mater*. 2018;30(18):6259-6276.

127. Wang P, Qu WJ, Song WL, Chen HS, Chen RJ, Fang DN. Electro-chemo-mechanical issues at the interfaces in solid-state lithium metal batteries. *Adv Funct Mater*. 2019;29(27): 1900950.

128. Persson BNJ. Contact mechanics for randomly rough surfaces. *Surf Sci Rep*. 2006;61(4):201-227.

129. Tian HK, Qi Y. Simulation of the effect of contact area loss in all-solid-state Li-ion batteries. *J Electrochem Soc*. 2017;164(11): E3512-E3521.

130. Koerver R, Aygun I, Leichtweiss T, et al. Capacity fade in solid-state batteries: interphase formation and chemomechanical processes in nickel-rich layered oxide cathodes and lithium thiophosphate solid electrolytes. *Chem Mater*. 2017;29(13): 5574-5582.

131. Lee H, Oh P, Kim J, et al. Advances and prospects of sulfide all-solid-state lithium batteries via one-to-one comparison with conventional liquid lithium ion batteries. *Adv Mater*. 2019;31(29):1900376.

132. Hu Y-S. Batteries: Getting solid. *Nat Energy*. 2016;1(4):16042.

133. Chung H, Kang B. Mechanical and thermal failure induced by contact between a $Li_{1.5}Al_{0.5}Ge_{1.5}(PO_4)_3$ solid electrolyte and Li metal in an all solid-state Li cell. *Chem Mater*. 2017;29(20): 8611-8619.

134. Kaboli S, Girard G, Zhu W, et al. Thermal evolution of NASICON type solid-state electrolytes with lithium at high temperature via in situ scanning electron microscopy. *Chem Commun*. 2021;57(84):11076-11079.

135. Huo HY, Luo J, Thangadurai V, Guo XX, Nan CW, Sun XL. Li_2CO_3: a critical issue for developing solid garnet batteries. *ACS Energy Lett*. 2020;5(1):252-262.

136. Sharafi A, Kazyak E, Davis AL, et al. Surface chemistry mechanism of ultra-low interfacial resistance in the solid-state electrolyte $Li_7La_3Zr_2O_{12}$. *Chem Mater*. 2017;29(18): 7961-7968.

137. Alexander GV, Patra S, Valiyaveetil S, et al. Electrodes-electrolyte interfacial engineering for realizing room temperature lithium metal battery based on garnet structured solid fast Li^+ conductors. *J Power Sources*. 2018;396: 764-773.

138. Feng WL, Dong XL, Li PL, Wang YG, Xia YY. Interfacial modification of Li/garnet electrolyte by a lithiophilic and breathing interlayer. *J Power Sources*. 2019;419:91-98.

139. Luo W, Gong YH, Zhu YZ, et al. Transition from superlithiophobicity to superlithiophilicity of garnet solid-state electrolyte. *J Am Chem Soc*. 2016;138(37):12258-12262.

140. Luo W, Gong YH, Zhu YZ, et al. Reducing interfacial resistance between garnet-structured solid-state electrolyte and Li-metal anode by a germanium layer. *Adv Mater*. 2017;29(22): 1606042.

141. He MH, Cui ZH, Chen C, Li YQ, Guo XX. Formation of self-limited, stable and conductive interfaces between garnet electrolytes and lithium anodes for reversible lithium cycling in solid-state batteries. *J Mater Chem A*. 2018;6(24): 11463-11470.

142. Lu Y, Huang X, Ruan YD, et al. An in situ element permeation constructed high endurance Li-LLZO interface at high current densities. *J Mater Chem A*. 2018;6(39):18853-18858.

143. Duan J, Wu WY, Nolan AM, et al. Lithium-graphite paste: an interface compatible anode for solid-state batteries. *Adv Mater*. 2019;31(10):1807243.

144. Tsai CL, Roddatis V, Chandran CV, et al. $Li_7La_3Zr_2O_{12}$ interface modification for Li dendrite prevention. *ACS Appl Mater Inter*. 2016;8(16):10617-10626.

145. Liu T, Ren YY, Shen Y, Zhao SX, Lin YH, Nan CW. Achieving high capacity in bulk-type solid-state lithium ion battery based on $Li_{6.75}La_3Zr_{1.75}Ta_{0.25}O_{12}$ electrolyte: interfacial resistance. *J Power Sources*. 2016;324:349-357.

146. Xiao Y, Turcheniuk K, Narla A, et al. Electrolyte melt infiltration for scalable manufacturing of inorganic all-solid-state lithium-ion batteries. *Nat Mater*. 2021;20(7):984-990.

147. Fu KK, Gong YH, Liu BY, et al. Toward garnet electrolyte-based Li metal batteries: an ultrathin, highly effective, artificial solid-state electrolyte/metallic Li interface. *Sci Adv*. 2017; 3(4):e1601659.

148. Zhang WB, Schroder D, Arlt T, et al. (Electro) chemical expansion during cycling: monitoring the pressure changes in operating solid-state lithium batteries. *J Mater Chem A*. 2017; 5(20):9929-9936.

149. McGrogan FP, Swamy T, Bishop SR, et al. Compliant yet brittle mechanical behavior of $Li_2S-P_2S_5$ lithium-ion-conducting solid electrolyte. *Adv Energy Mater*. 2017;7(12):1602011.

150. Bucci G, Swamy T, Chiang Y-M, Carter WC. Modeling of internal mechanical failure of all-solid-state batteries during electrochemical cycling, and implications for battery design. *J Mater Chem A*. 2017;5(36):19422-19430.

151. Jin E, Tantratian K, Zhao C, et al. Ionic conductive and highly-stable interface for alkali metal anodes. *Small.* 2022; 18(33):e2203045.

152. Takada K, Ohta N, Zhang LQ, et al. Interfacial phenomena in solid-state lithium battery with sulfide solid electrolyte. *Solid State Ion.* 2012;225:594-597.

153. Takada K. Progress and prospective of solid-state lithium batteries. *Acta Mater.* 2013;61(3):759-770.

154. Zhu YZ, He XF, Mo YF. Origin of outstanding stability in the lithium solid electrolyte materials: insights from thermodynamic analyses based on first-principles calculations. *ACS Appl Mater Inter.* 2015;7(42):23685-23693.

155. Richards WD, Miara LJ, Wang Y, Kim JC, Ceder G. Interface stability in solid-state batteries. *Chem Mater.* 2016;28(1): 266-273.

156. Nolan AM, Wachsman ED, Mo YF. Computation-guided discovery of coating materials to stabilize the interface between lithium garnet solid electrolyte and high-energy cathodes for all-solid-state lithium batteries. *Energy Storage Mater.* 2021;41: 571-580.

157. Miara LJ, Richards WD, Wang YE, Ceder G. First-principles studies on cation dopants and electrolyte|cathode interphases for lithium garnets. *Chem Mater.* 2015;27(11):4040-4047.

158. Zhu YZ, He XF, Mo YF. First principles study on electrochemical and chemical stability of solid electrolyte-electrode interfaces in all-solid-state Li-ion batteries. *J Mater Chem A.* 2016; 4(9):3253-3266.

159. Sang LZ, Bassett KL, Castro FC, et al. Understanding the effect of interlayers at the thiophosphate solid electrolyte/lithium Interface for all-solid-state Li batteries. *Chem Mater.* 2018;30(24):8747-8756.

160. Li XF, Liu J, Banis MN, et al. Atomic layer deposition of solid-state electrolyte coated cathode materials with superior high-voltage cycling behavior for lithium ion battery application. *Energ Environ Sci.* 2014;7(2):768-778.

161. Koc T, Hallot M, Quemin E, et al. Toward optimization of the chemical/electrochemical compatibility of halide solid electrolytes in all-solid-state batteries. *ACS Energy Lett.* 2022;7(9): 2979-2987.

162. Bates JB, Dudney NJ, Neudecker BJ, Hart FX, Jun HP, Hackney SA. Preferred orientation of polycrystalline $LiCoO_2$ films. *J Electrochem Soc.* 2000;147(1):59-70.

163. Takeuchi S, Tan HY, Bharathi KK, et al. Epitaxial $LiCoO_2$ films as a model system for fundamental electrochemical studies of positive electrodes. *ACS Appl Mater Inter.* 2015; 7(15):7901-7911.

164. Nishio K, Nakamura N, Horiba K, et al. Impact of the crystal orientation of positive electrodes on the Interface resistance across a solid electrolyte and electrode. *ACS Appl Energ Mater.* 2020;3(7):6416-6421.

165. Waqas M, Ali S, Chen DJ, et al. A robust bi-layer separator with Lewis acid-base interaction for high-rate capacity lithium-ion batteries. *Compos Part B-Eng.* 2019;177: 107448.

166. Nolan AM, Zhu YZ, He XF, Bai Q, Mo YF. Computation-accelerated design of materials and interfaces for all-solid-state lithium-ion batteries. *Joule.* 2018;2(10):2016-2046.

167. Shi SQ, Gao J, Liu Y, et al. Multi-scale computation methods: their applications in lithium-ion battery research and development. *Chinese Phys B.* 2016;25(1):018212.

AUTHOR BIOGRAPHIES

Huaihu Sun is a PhD candidate at the Institut National de la Recherche Scientifique (INRS), center for Energy, Materials, and Telecommunications, Canada. His research focuses on interface engineering for solid-state batteries.

Gaixia Zhang is a professor and Canada Research Chair at École de Technologie Supérieure (ÉTS), University of Quebec, Montréal, Canada. She received her PhD degree from Polytechnique Montréal, and then continued her research at Western University and INRS, Canada. Her research interests focus on advanced materials (catalysts, electrodes, and electrolytes) for sustainable energy conversion and storage applications, including batteries, fuel cells, hydrogen production, and CO_2 reduction. She is also interested in interface and device engineering, as well as in situ characterizations and theoretical simulations.

Shuhui Sun is a full professor at the Institut National de la Recherche Scientifique (INRS), center for Energy, Materials, and Telecommunications, Canada. He is a Fellow of the Royal Society of Canada (RSC), and a Fellow of the Canadian Academy of Engineering (CAE). His current research interests focus on multifunctional nanomaterials for energy conversion and storage applications, including H_2 fuel cells, metal-ion (Li-, Na-, and Zn-ion) batteries, lithium-metal batteries, metal-air batteries, solid-state batteries, and so on. He is also interested in nanostructured photo- and electro-catalysts for H_2 production, CO_2 reduction, and water treatment.